Title
High spatial-resolution satellite mapping of suspended particulate matter in global coastal waters using particle composition-adaptive algorithms

Authors
Teng, Wenxiu
Yu, Qian
Stramski, Dariusz
et al.

Publication Date
2025-06-01

DOI
10.1016/j.rse.2025.114745

High Spatial-Resolution Satellite Mapping of Suspended Particulate Matter in Global Coastal Waters Using Particle Composition-Adaptive Algorithms

Wenxiu Teng [a*], Qian Yu [a], Dariusz Stramski [b], Rick A. Reynolds [b], Jonathan D. Woodruff [a], Brian Yellen [a]

[a] Department of Earth, Geographic, and Climate Sciences, University of Massachusetts Amherst, Amherst, MA, USA
[b] Marine Physical Laboratory, Scripps Institution of Oceanography, University of California San Diego, CA, USA

Corresponding author: Wenxiu Teng (wteng@umass.edu)

Abstract

Delivery of suspended particles, referred hereafter also to as suspended sediment, to coastal zones plays a first order control on the development and maintenance of muddy geomorphic features like river deltas, mudflats, and tidal wetlands. While sediment delivery from rivers is relatively straightforward to monitor and has been well studied, suspended sediment derived from erosion of coastal bluffs and resuspension of shallow subtidal sediments remains poorly constrained. Estimates of the concentration of suspended particulate matter (SPM) provide one of the best remotely sensed metrics for suspended sediment supply to the coast. Spaceborne ocean color sensors with coarse spatial resolution (~1 km pixel size at nadir) are generally inadequate to resolve smaller-scale sediment dynamics in coastal waters and additionally there is a limitation associated with adjacency effect of 1-km land pixels on near-shore water pixels. In contrast, satellites dedicated primarily to land observations with a smaller pixel size (~30 m) provide more adequate spatial resolution for observations of coastal waters. This paper presents a particle composition adaptive algorithm for retrieving SPM from ocean remote-sensing reflectance, $R_{rs}(\lambda)$, in coastal waters which is applicable to most land observation satellites. For the algorithm development, we compiled more than 800 paired in situ spectral reflectance and SPM measurements from 12 marine sites worldwide, representing a wide range of suspended particle concentration and composition. We first classify the satellite image data into three water types: organic-rich, mineral-rich, or extremely mineral-rich based on the POC/SPM ratio that is derived from $R_{rs}(\lambda)$. The ratio of particulate organic carbon (POC) to SPM serves as a particle composition metric. Then, SPM is estimated from $R_{rs}(\lambda)$ using a particle composition-specific algorithm which employs the reflectance at red band for organic-rich waters and near-infrared (NIR) for mineral-rich waters. We compared the performance of this algorithm with eight previously published SPM algorithms, including empirical, semi-analytical, and machine learning approaches. Results show that our algorithm produces reliable SPM estimation with coefficient of determination (R^2), root mean square error (RMSE in log space), and median absolute percent error (MAPE) of 0.91, 0.20, and 30.5%, respectively. To examine the capability of our algorithm to study the long-term variability in coastal SPM at high spatial resolution, we implemented the algorithm to the 40-year Landsat data archive in Google Earth Engine (GEE). The Landsat mapping results of SPM were validated using both the satellite-in situ matchups of SPM data as well as in situ water turbidity measurements. Finally, we demonstrate a few scenarios of fine-scale SPM patterns as well as seasonal and long-term variability across different marine coastal environments using the satellite high spatial resolution SPM mapping. These results collectively demonstrate the promise of this new SPM retrieval algorithm for mapping and monitoring global coastal suspended sediment dynamics.

Keywords

Remote sensing, coastal sediment dynamics, suspended particulate matter, particle composition, water type classification, Landsat, Google Earth Engine (GEE)

1. Introduction

Coastal landscapes, such as beaches, tidal wetlands, and mudflats, provide essential ecosystem services, including supporting biodiversity, storing blue carbon, and offering natural defenses against storm surges (Barbier et al. 2011; Hopkinson et al. 2019; Windham-Myers et al. 2018). These landscapes depend on a continuous supply of sediment from various sources, such as rivers and coastal erosion, to maintain accretion rates and protect the integrity of these landscapes in the face of different pressures, such as sea level rise (SLR) and the increased intensity and frequency of coastal flood events (Coleman et al. 2022; Fagherazzi et al. 2013; Kirwan and Megonigal 2013; Ladd et al. 2019). For example, adequate sediment supply allows tidal wetlands to continuously sequester carbon in their sediments through vertical accretion, allowing them to keep up with gradual SLR and auto-compaction. (Allen 2000; Cahoon et al. 2019; Fagherazzi et al. 2020; Kirwan and Guntenspergen 2012; Mudd et al. 2004). Numerous studies have shown that a sediment deficit leads to marsh degradation under current rates of SLR (Ganju et al. 2017; Peteet et al. 2018; Weston 2013). Understanding coastal sediment dynamics is vital for managing these landscapes and maintaining their ecosystem services, particularly carbon sequestration.

Coastal landscapes that rely heavily on river sediment supplies are increasingly threatened by reduced riverine sediment due to upstream damming and channelization, compounded by rising sea levels (Meade and Moody 2009; Syvitski and Kettner 2011; Walling 2008; Weston 2013). A recent study evaluating the contribution of river sediment to the maintenance of coastal wetlands found that nearly half of the tidal wetlands in the conterminous US would require ten times more sediment than rivers currently supply in order to keep pace with sea level rise (Ensign et al. 2023). This suggests that watershed-derived sediment is relatively minor for many coastal systems compared to marine sources, with coastal erosion likely serving as a key sourcing mechanism and major contributor to tidal wetland accretion. This is particularly true in areas with low river sediment supply; for instance, in the Northeast US, where the absence of major deltaic systems means that salt marshes predominantly rely on the erosion of nearshore glacial sediment deposits by storms and high wave activity offshore (Baranes et al. 2022; Hopkinson et al. 2018; Yellen et al. 2023).

Despite the recognized importance of sediment supply from coastal erosion (Ensign et al. 2023; O'Connell 2010), research in this area remains disproportionately understudied compared to the extensive research conducted on river sediments (Fagherazzi et al. 2020). The magnitude of fluvial sediment supply and changes in flux have been extensively studied and have long been the focus of Earth science research (Milliman and Syvitski 1992). Rivers are easier to monitor because they have abundant bridge crossings on which to mount in situ sediment monitoring equipment. Furthermore, upstream of tides, mass fluxes in rivers (water and sediment) tend to be unidirectional, simplifying flux estimates. This research gap is mainly due to the difficulty of instrumenting coastal zones, where high wave and tide energy make measurements challenging (Fagherazzi et al. 2020). As a result, there are few large-scale studies estimating the magnitude of sediment supply to the coastal zone from non-fluvial sources, or assessing temporal changes due to human modifications of the coastline. The lack of coastal sediment observations hamper comprehensive understanding for the importance of marine-derived sediment to coastal systems (particularly fine-grained sediments to back barrier tidal wetlands), as well as the impact of human structures and climate induced changes that might govern this delivery.

Satellite ocean color remote sensing can help overcome some of the challenges associated with assessing coastal suspended sediment using more direct but logistically challenging field measurements (Volpe et al. 2011; Zhang et al. 2020) (Fig. 1). There are two main types of satellite sensors commonly used to map the concentration of suspended particulate matter (SPM): ocean color sensors and land observation sensors. Ocean color sensors, such as MODIS, typically offer optical measurements at multiple spectral bands in the visible and near-infrared (NIR) spectral regions, allowing to capture main spectral features of ocean reflectance associated with SPM and other water constituents (Fig. S1a). However, the coarse spatial resolution (e.g., ~1 km) of these sensors limits their effectiveness in mapping sediment dynamics in littoral zones where spatial scales of variability are often smaller than 1 km and the adjancency effect of land and mixed land/ocean pixels impose further limations on the imaged data (Fig. 2). In contrast, land observation sensors, like those in the Landsat series operational since 1984, provide higher spatial resolution (30 m), which is more adequate for resolving the smaller-scale variability of coastal suspended sediment and minimizing the land adjancency effects (Fig. 2). However, these sensors have lower spectral resolution, for instance, Landsat has fewer bands and broader bandwidths in the visible and NIR regions (Fig. S1a) compared to MODIS. This limitation raises questions about their ability to accurately estimate SPM concentration, especially in view of variability in the optical properties of SPM associated with variable composition of suspended particulate matter.

The complexity of coastal SPM composition poses challenges for remote sensing monitoring. SPM includes inorganic particles (e.g., clay and silt), as well as living and non-living particulate organic matter (e.g., phytoplankton and detritus). These components originate from various sources, including fluvial discharge, shoreline soil erosion, tidal wetland degradation, local bottom resuspension, and phytoplankton production (Boss et al. 2001; Ganju et al. 2017; Milliman 1997; Sweet et al. 2022) (Fig. 1). The contributions of these sources vary with tidal dynamics, seasonal changes, and episodic events like cyclonic storms (Cortese et al. 2024; Walker 2001). Consequently, the water column often contains a dynamic mix of organic and inorganic particles with notable variations in concentration, chemical composition, and size (Bianchi 2011; Miller and McKee 2004; Stramski et al. 2004). All these factors influence the light absorption and scattering properties of SPM, and hence the ocean spectral remote-sensing reflectance, $R_{rs}(\lambda)$ where λ is light wavelength in vacuum (Gordon 2019; Kirk 1994; Mobley 2022), making it challenging to accurately estimate SPM from $R_{rs}(\lambda)$ in optically complex coastal waters.

Over the last few decades, several algorithms have been developed to retrieve SPM from remote-sensing reflectance, including empirical, semi-analytical, and machine learning algorithms (Balasubramanian et al. 2020; Doxaran et al. 2002; Han et al. 2016; Jiang et al. 2021). These algorithms are designed either for specific sites or applications on regional and global scales. Site-specific studies often use single-band or simple reflectance band-ratio algorithms, which provide reasonably accurate estimates within limited SPM ranges. For example, Miller and McKee (2004) used linear regression with MODIS-Terra red band to map SPM in the Mississippi River Delta, and Doxaran et al. (2002) used visible and NIR band ratios to map SPM in turbid waters of the Gironde estuary. While potentially effective for specific sites, these algorithms are unlikely to perform well across diverse aquatic environments due to the optical complexity and variability of water constituents, especially the suspended particulate matter (Stramski et al. 2023).

To address these challenges, adaptive optical water type (OWT) classification approaches have emerged as a promising framework for developing generalized algorithms that can be applied across various aquatic environments, from open oceans and coastal areas to inland waters (Balasubramanian et al. 2020; Bi and Hieronymi 2024; Jiang et al. 2021; Mélin and Vantrepotte 2015; Moore et al. 2001). These adaptive classification approaches, which utilize spectral shape or magnitude of reflectance to distinguish water types, have significant potential to improve the overall retrieval accuracy of optically-significant constituents across a wide range of water bodies and to advance a unified approach for global applications. For example, Balasubramanian et al. (2020) classified water into three classes including blue-green water, green water, and brown water across diverse samples from rivers, lakes, estuaries, and coastal waters, and then estimated SPM using semi-analytical, machine-learning, and empirical algorithms. Jiang et al. (2021) classified waters into four water turbidity types and then estimated SPM separately using semi-analytical algorithms with both inland and coastal waters data. However, the spectral bands of $R_{rs}(620)$ and $R_{rs}(754)$ used in their study are not available on most land observation satellites, such as Landsat. Dethier et al. (2020) used unsupervised K-means clustering to account for river-to-river variability and enhance SPM prediction accuracy. However, their approach was designed specifically for rivers and calibrated for Landsat using field-measured SPM data, which limits its applicability to other water types and satellites.

In contrast to classifications based on ocean reflectance spectra, Stramski et al. (2023) proposed a novel adaptive approach for ocean color algorithms which accounts for variations in composition of suspended particulate matter. Specifically, the ratio of particulate organic carbon POC to SPM (POC/SPM) concentrations has been used as a measure of composition of particulate matter to characterize the varying proportion of organic and inorganic particles. The optical reflectance-based algorithms were formulated to estimate POC/SPM using field data collected in Arctic waters. The optically-derived POC/SPM then served as a basis of adaptive ocean color algorithms for estimating POC across a broad range of varying particle concentration and composition within the Arctic marine environments. The methodology of this adaptive framework, formulation of algorithms, and example application were demonstrated for several past and presently operating satellite multispectral ocean color sensors which provide data at a nominal ~1 km spatial resolution.

Despite advancements in SPM retrieval algorithms, most existing algorithms are tailored to ocean color satellites and are not directly applicable to land observation satellites which have significantly higher spatial resolution that is required to capture coastal sediment dynamics but are more limited in terms of spectral measurement characteristics. Additionally, many existing SPM algorithms are not specifically designed for coastal waters that exhibit diverse and variable organic and inorganic compositions from various sources and processes, making accurate SPM mapping challenging. In this study, we developed a new SPM algorithm intended for improved estimation of SPM across global coastal waters. This algorithm is designed for use with land observation satellites to enable long-term high spatial resolution mapping of SPM and provide a better understanding of sediment dynamics in coastal environments.

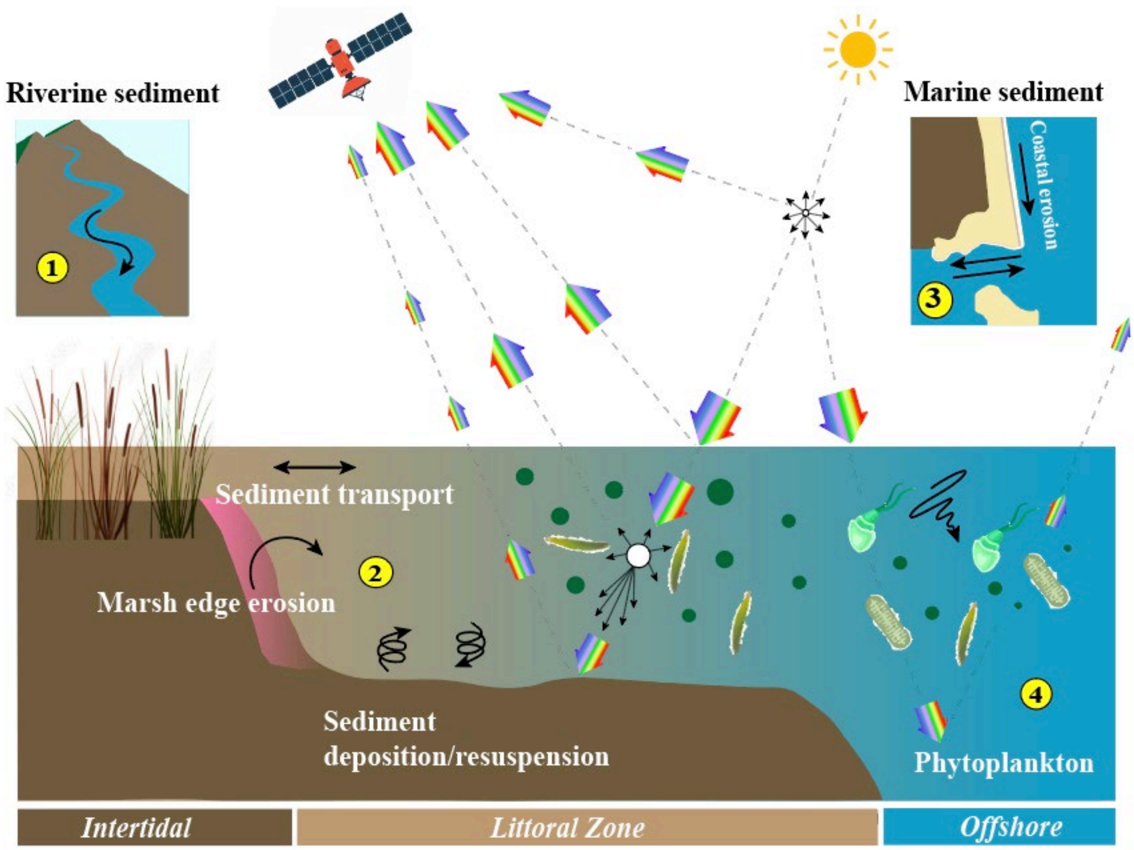

Figure 1. The interaction of light with suspended sediments, phytoplankton, organic detritus, colored dissolved organic matter, and water molecules plays a crucial role in determining remotely sensed ocean color. This diagram illustrates how light interacts with suspended particles originating from various sources, including riverine sediment (1), marsh edge erosion and local resuspension (2), marine sediment from coastal erosion (3), and phytoplankton (4).

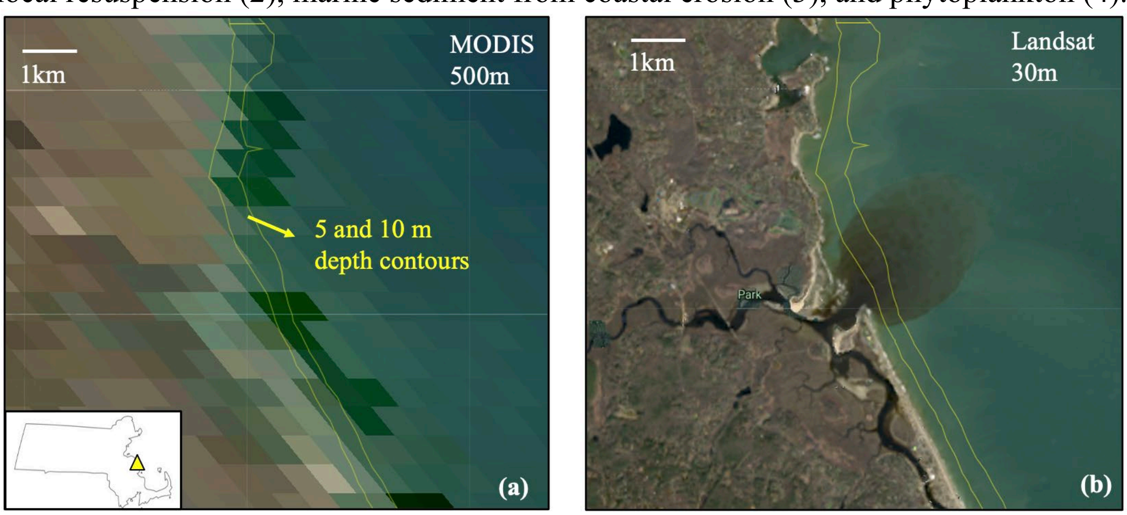

Figure 2. Comparison between an ocean color sensor (MODIS) and a land observation sensor (Landsat). (a) MODIS-Terra Surface Reflectance on Google Earth Engine (GEE) (b) Landsat 8 Surface Reflectance on GEE. Both images are displayed in true color.

2. Data and Methods

2.1 Study area and datasets

2.1.1 In situ ocean reflectance spectra, SPM, and POC data

To develop a global SPM retrieval algorithm, we compiled a high-quality in situ dataset to capture the variability of optical water types in coastal waters. Several datasets, including GLORIA (Lehmann et al. 2023), Delta-X (Fichot and Harringmeyer 2023), Belgian coastal zone (Castagna et al. 2022), and Arctic dataset (Stramski et al. 2023), provided in situ spectral reflectance paired with measurements of SPM and POC on surface water samples. In this paper, we use the term "suspended particulate matter" (SPM) instead of "total suspended solids" or "total suspended sediment" (TSS) to maintain scientific accuracy and avoid misleading terminology. The standard gravimetric method involves filtering water through a pre-weighed filter (e.g., GF/F glass-fiber), then drying and reweighing to determine particle mass. This method does not capture all particles, as submicron particles can pass through the filter. Thus, "total" can be misleading because not all particles are included in the measurement of particle mass. Using "SPM" provides a more reasonable representation of the measurement methodology and avoids potentially misleading interpretation of the word "total".

Our data compilation encompassed 12 research sites worldwide, representing a diverse array of marine coastal settings (see Fig. 3 and Table 1). Of these, four sites are located near river outlets and as such, predominantly affected by riverine sediment export. Six sites are located further offshore, or along coasts devoid of major rivers or wetland complexes where suspended particles are largely derived from coastal erosion or phytoplankton growth. Two sites are influenced by tidal marshes, located either in tidal marsh-influenced estuaries or near marsh platforms, with sediments primarily sourced from marsh and estuary/coastal exchanges. The classification of coastal settings only indicates the sources of SPM and is not used for water type classification. In situ $R_{rs}(\lambda)$ was measured within the 350 to 900 nm wavelength range, although due to instrumental and processing constraints some spectra were limited to the 400 to 750 nm range. Water samples for SPM and POC determinations were collected at near-surface depths (0–5 m), primarily near the coast where a mix of organic and inorganic sediments from river, marsh, or marine sources are present. The final dataset in this study includes over 800 in situ spectral reflectance observations paired with SPM measurements.

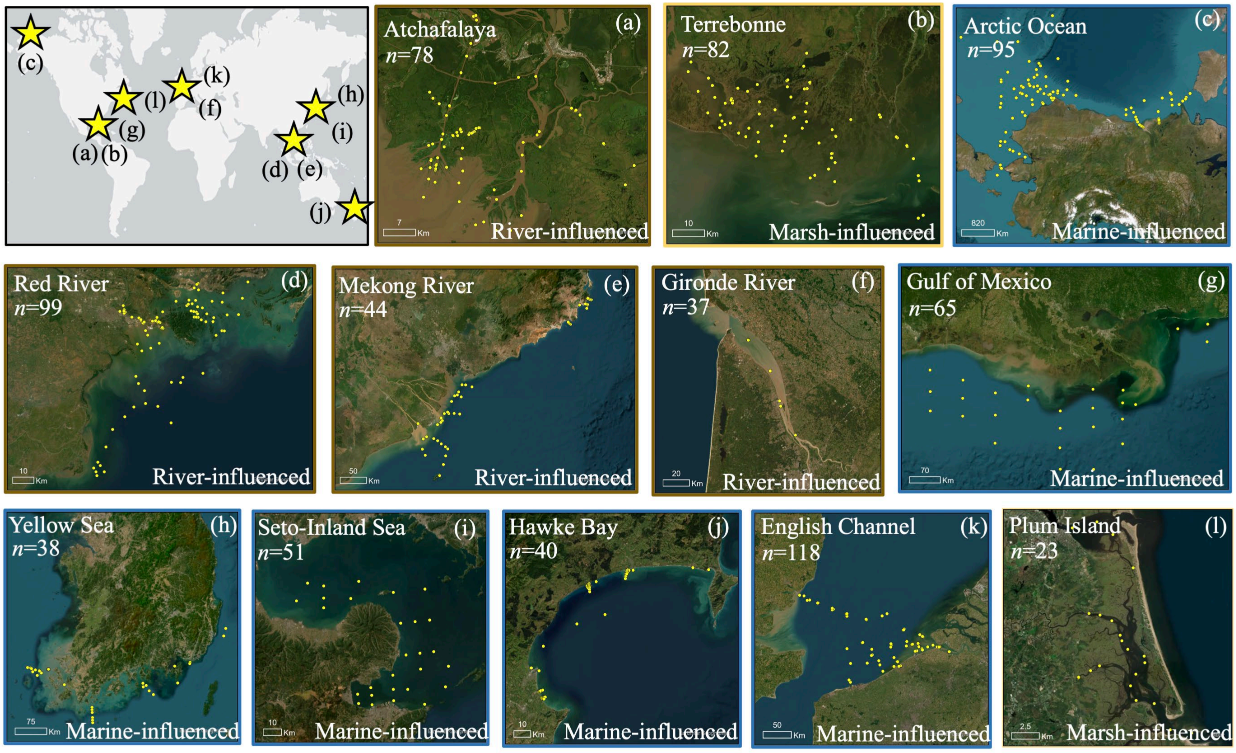

Figure 3. The geographical distributions of the compiled in situ datasets. Each panel shows the locations of in situ measurements in yellow dots for different study sites. The number of samples (*n*) is indicated for each site, along with the sediment source type (river-influenced, marsh-influenced, or marine-influenced). (a) Atchafalaya River, (b) Terrebonne Basin, (c) Arctic Ocean, (d) Red River, (e) Mekong River, (f) Gironde River, (g) Gulf of Mexico, (h) Yellow Sea, (i) Seto-Inland Sea, (j) Hawke Bay, (k) English Channel, and (l) Plum Island.

Table 1. Range and median (in parentheses) of field SPM and POC measurements (in units of g/m^3) for each site with information on the sediment source, the total number of in situ samples collected, the number of samples used for SPM algorithm development, the number of samples matched with satellite image data, and the sources of the data.

Location	SPM [g/m^3]	POC [g/m^3]	POC/SPM [%]	Sediment source	*n* (total)	*n* (algorithm calibration)	*n* (matched with image)	Source
Atchafalaya River, LA	6.58-154.50 (33.17)	0.53-4.57 (1.45)	0.014-0.159 (0.030)	River-influenced	78	39	-	Fichot & Harringmeyer, 2023
Mekong River	0.47-10.69 (1.83)	-	-	River-influenced	44	-	-	Lehmann et al., 2023
Red River	1.09-147.69 (10.39)	-	-	River-influenced	99	-	-	Lehmann et al., 2023
Gironde River	44.51-1815.35 (229.59)	-	-	River-influenced	37	19	-	Lehmann et al., 2023

Terrebonne Basin, LA	2.20-90.10 (28.50)	0.31-4.87 (2.18)	0.018-0.232 (0.058)	Marsh-influenced	82	41	9	Fichot & Harringmeyer, 2023
Plum Island, MA	1.02-21.71 (7.65)	-	-	Marsh-influenced	23	-	9	Lehmann et al., 2023
Arctic Ocean	0.044-20.62 (0.37)	0.02-1.02 (0.13)	0.015-0.583 (0.322)	Marine-influenced	95	47	2	Stramski et al., 2023
English Channel	0.333-118.33 (4.73)	-	-	Marine-influenced	118	-	-	Castagna et al., 2022; Lehmann et al., 2023
Yellow Sea	0.26-110.24 (5.08)	-	-	Marine-influenced	38	-	-	Lehmann et al., 2023
Seto-Inland Sea	0.25-6.40 (0.98)	-	-	Marine-influenced	51	-	2	Lehmann et al., 2023
Gulf of Mexico, LA	0.087-8.63 (0.82)	-	-	Marine-influenced	65	-	-	Lehmann et al., 2023
Hawke Bay	1.53-77.92 (16.28)	-	-	Marine-influenced	40	-	-	Lehmann et al., 2023

The spectral curves of $R_{rs}(\lambda)$ exhibit diverse shapes and magnitudes (see §3.2.1 for details). The SPM data we compiled range from very clear waters with SPM = 0.04 g/m^3 to highly turbid waters with SPM = 1815 g/m^3, spanning more than five orders of magnitude. The POC/SPM ratio varied significantly across sites from 0.01 to 0.6, covering approximately the full range that can be expected for this particulate compositional metric in natural waters (Stramski et al. 2023). Particle assemblages ranged from being dominated by mineral particles (like Atchafalaya, with a median POC/SPM of 0.03), to a mix of mineral and organic particles (like Terrebonne, with a median POC/SPM of 0.058), and organic-dominated (like Arctic Ocean data, with a median POC/SPM of 0.322). Across different environments, the river- and marsh-influenced sites exhibit higher levels of SPM compared to marine-influenced environments (Fig. 4). The POC levels increase progressively from marine-influenced to river-influenced, and finally to marsh-influenced environments. The POC/SPM ratio increases from river-influenced to marsh-influenced, and then to marine-influenced environments.

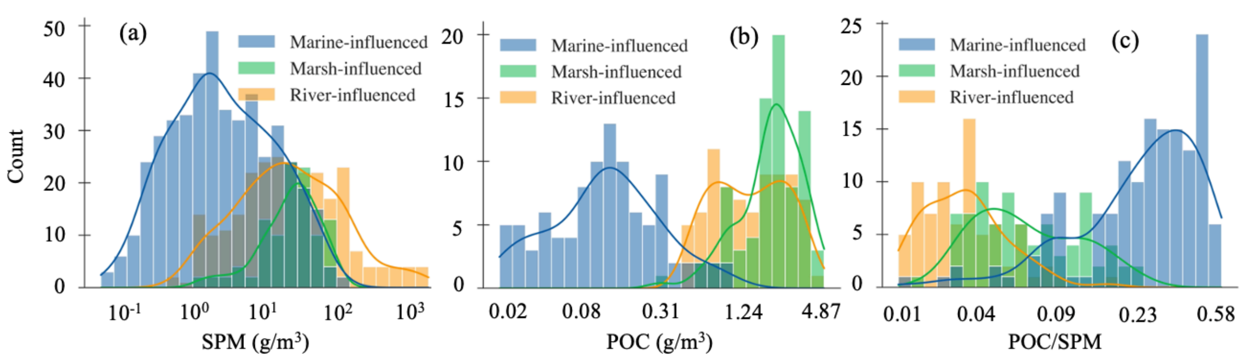

Figure 4. Probability distribution of (a) SPM, (b) POC and (c) POC/SPM in marine-influenced, marsh-influenced, and river-influenced waters.

Overall, the extensive variability of geographical locations (Fig. 3), spectral characteristics (see Fig. 7 in §3.2.1), SPM concentration, and particle composition (Table 1 and Fig. 4) illustrates the diverse scenarios represented by our compiled datasets. These scenarios range from very clear to extremely turbid waters, featuring highly variable particle compositions influenced by different sources such as rivers, marshes, and marine systems.

2.1.2 Landsat imagery and atmospheric correction

To apply our newly developed SPM algorithm to satellite data for demonstration purposes and for future studies of coastal suspended sediment, we used the Landsat historical catalog that dates back to 1984. Landsat's 30-m spatial resolution data make it generally adequate for mapping fine-scale spatial patterns of coastal sediment transport and the Landsat long history allow for detecting long-term temporal trends in coastal SPM patterns. We used the Google Earth Engine (GEE) cloud platform to access Level-2 Collection 2 Surface Reflectance Science Product imagery from the U.S. Geological Survey. Our dataset includes Landsat 5 (1984–2012), Landsat 7 (1999–2022), Landsat 8 (2013–present), and Landsat 9 (2021–present) (Fig. S1b). These four sensors have provided Earth observation data since 1984 with a 30-m spatial resolution and 16-day temporal repeat cycle. The overlapping operational periods of these satellites have decreased the effective revisit time to 8 days since 1999.

To minimize the impact of cloud contamination on satellite imagery, we excluded images with cloud cover exceeding 30% as indicated by the Quality Assessment (QA) band. Additionally, we applied a bitmask to the 'QA_PIXEL' band to isolate high-quality pixels, effectively excluding those compromised by fill, dilated clouds, clouds including cirrus, and cloud shadows. In order to mask out land pixels and those with a mixture of land and water, we used the JRC Global Surface Water dataset (Pekel et al. 2016) with the following thresholds: water occurrence greater than 90%, transition less than 2, water seasonality greater than 11, and water recurrence greater than 90%. Additionally, we masked out pixels with a normalized difference water index (NDWI) (McFeeters 1996) of less than 0.5 to further refine the delineation of water extent in each image.

The Landsat Level-2 Surface Reflectance (SR) was atmospherically corrected using the Landsat Ecosystem Disturbance Adaptive Processing System (LEDAPS) algorithm (version 3.4.0) for Landsat 5 and Landsat 7, and the Land Surface Reflectance Code (LaSRC) algorithm (version 1.5.0) for Landsat 8 and Landsat 9 (Skakun et al. 2019; Wolfe et al. 2004). Both algorithms effectively correct for atmospheric contributions to top-of-atmosphere radiance measured by the satellite sensor, such as aerosols and water vapor, across different times, locations, and spectral ranges. However, it is important to note that these atmospheric correction methods are designed for terrestrial applications and do not correct for skylight reflection at the air-water interface, potentially introducing an error in estimates of remote-sensing reflectance $R_{rs}(\lambda)$, which must be addressed before the application of SPM retrieval algorithm.

Empirical line method was used to correct for light reflected at the air-water interface. We first paired concurrent field-measured $R_{rs}(\lambda)$ with Landsat SR data from our compiled datasets (Table 1). Given the dynamic nature of coastal waters, strict criteria were applied to the dataset pairing: (i) Landsat SR was centered on a single pixel (30m x 30m) at the in situ sampling location; (ii) the field $R_{rs}(\lambda)$ was measured within ±2 hours of the Landsat overpass between 8:00 AM and 12:00 PM local time; (iii) pixels affected by cloud/haze, shadows, or snow/ice were excluded; and (iv) to avoid contamination from land adjacency effects and bottom reflectance, pixels along the edges of the main channel or in narrow channels (less than 100 m), close to land (< 20 m), or in shallow waters (< 0.5 m) were also removed. Using these criteria, we obtained high-quality field-measured $R_{rs}(\lambda)$ and Landsat SR matchups from our compiled dataset of 22 matchups (see Table 1), resulting in 14 matched data pairs. We used these data to build a relationship between field-measured $R_{rs}(\lambda)$ and Landsat SR, which was then used to correct the Landsat SR to obtain $R_{rs}(\lambda)$ in GEE.

2.2 SPM retrieval algorithms

The spectral remote-sensing reflectance $R_{rs}(\lambda)$ at wavelengths λ where particulate absorption is negligible or sufficiently weak is expected to increase with an increase in particle concentration in the water; however, this positive relationship is often influenced by particle composition (Jerlov 1976; Jonasz and Fournier 2007). Fig. 5 illustrates the $R_{rs}(\lambda)$ changes under constant SPM concentration while varying the POC/SPM ratio. At a given SPM concentration, particularly at longer wavelengths (e.g., 670 nm) where absorption by colored dissolved organic matter is minimal, $R_{rs}(\lambda)$ values tend to increase as the POC/SPM ratio decreases. This suggests that mineral-rich waters, which have a low POC/SPM ratio, exhibit higher $R_{rs}(\lambda)$. Consequently, a single predictive relationship cannot be universally applied across different particle composition categories to reliably estimate SPM from $R_{rs}(\lambda)$.

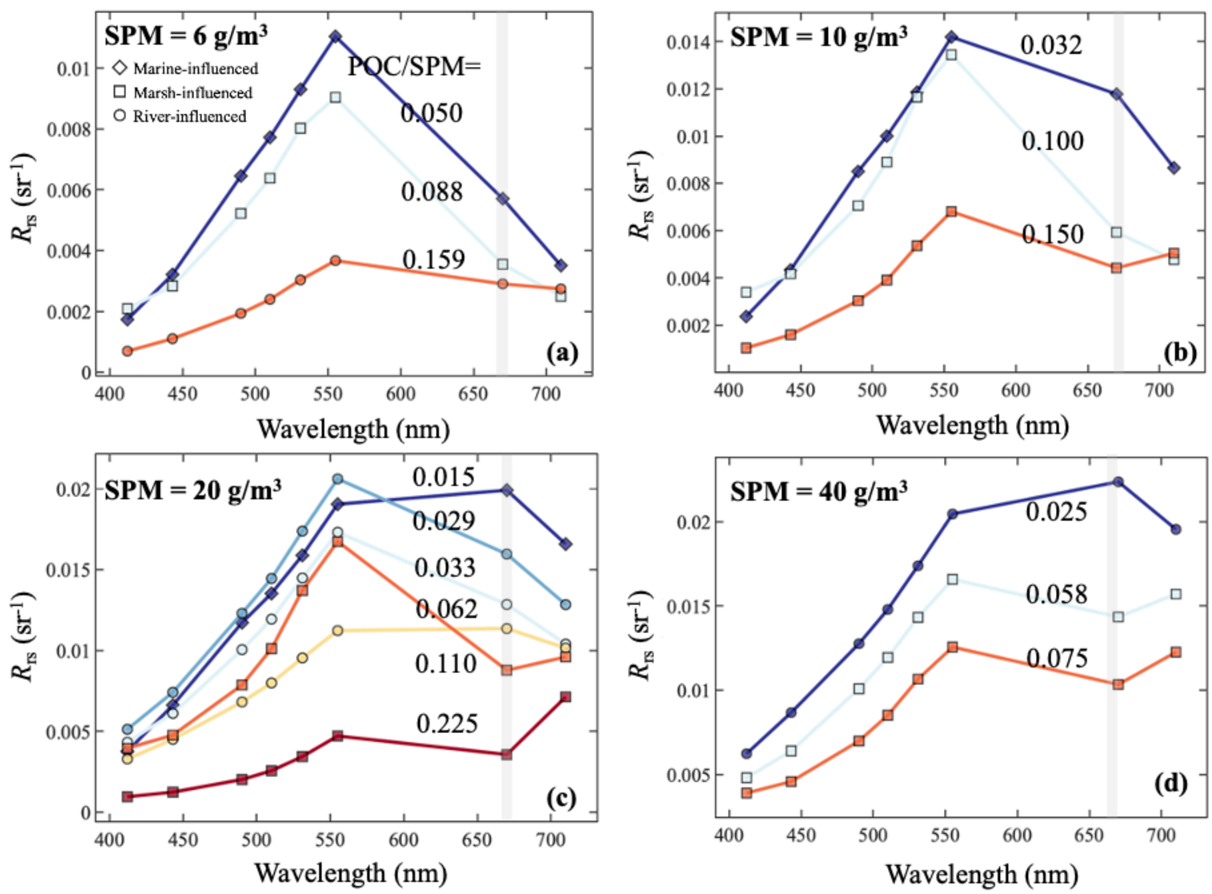

Figure 5. In situ spectral curve for constant SPM and varied POC/SPM ratio as labeled. (a) SPM = 6 g/m^3. (b) SPM = 10 g/m^3. (c) SPM = 20 g/m^3. (d) SPM = 40 g/m^3.

To improve SPM predictions, the proposed SPM algorithm is designed to account for the impact of varying POC/SPM ratios on spectral $R_{rs}(\lambda)$. Our approach involves two main steps: first, classifying water types based on POC/SPM ratios estimated from $R_{rs}(\lambda)$, and second, applying the particle composition-specific (i.e., POC/SPM-specific) algorithms to estimate SPM within each compositional class from $R_{rs}(\lambda)$.

We examined the estimation of POC/SPM using $R_{rs}(\lambda)$ (units of sr^{-1}) at one or multiple bands which is an adaptation of previous approach by Stramski et al. (2023):

$$\frac{\mathrm{POC}}{\mathrm{SPM}} = 10^{(a\ B + b)} \qquad (1)$$

$$\frac{\mathrm{POC}}{\mathrm{SPM}} = 10^{(a\ G + b)} \qquad (2)$$

$$\frac{\mathrm{POC}}{\mathrm{SPM}} = 10^{(a\ R + b)} \qquad (3)$$

$$\frac{\mathrm{POC}}{\mathrm{SPM}} = 10^{(a_1\ B + a_2\ G + a_3\ R + b)} \qquad (4)$$

where B is $\log[R_{rs}(\lambda_B)]$, G is $\log[R_{rs}(\lambda_G)]$, and R is $\log[R_{rs}(\lambda_R)]$ with λ_B = 490 nm, λ_G = 555 nm, and λ_R = 670 nm. The a and b are the best-fit coefficients of the single band regression model (Eq. 1-3). The $a_1, a_2, a_3, a_4,$ and b are the best-fit coefficients of the multiple band regression models (Eq. 4).

We chose the green band algorithm to estimate POC/SPM and classify water types because it provides the same overall water type classification accuracy as the three-bands algorithm (see §3.1 for details) while being simpler and more practical to implement. Based on the green band algorithm (Eq. 2), POC/SPM ratio is classified into three categories: organic-rich, mineral-rich, and extremely mineral-rich (E) as shown in Table 2. We optimized the boundary values for these classifications through a detailed correlation analysis between $R_{rs}(\lambda)$ and SPM, refining POC/SPM increments. The process for determining these boundary values is further detailed in §3.1.

Table 2. Classification rules for water type determination.

Water type class	Rule
Organic-rich	POC/SPM > 0.12 or $R_{rs}(670)$ < 0.01 sr^{-1}
Mineral-rich	0.02 < POC/SPM < 0.12
Extremely mineral-rich (E)	POC/SPM < 0.02

After classifying the water types based on particle composition, the next step is to estimate SPM from $R_{rs}(\lambda)$ using particle composition-specific algorithms for each compositional class. To determine which wavelength can serve as the best predictor of SPM for different water types, we fitted a linear regression between field-measured SPM and R_{rs} at many wavelengths within the range 400–890 nm. We found that the prediction accuracy varied significantly across wavelengths and displayed unique trends for each water type (see §3.2.2 for details). The red band provides better estimates for organic-rich particles, while the NIR band is more effective for mineral-rich and extremely mineral-rich particles. Therefore, we use these advantageous bands to retrieve SPM (units of g/m^3)for the three water types as follows:

$$\mathrm{SPM_{org}} = a\, R_{rs}(\lambda_{Red})^{\,b} \tag{5}$$

$$\mathrm{SPM_{min}} = a\, R_{rs}(\lambda_{NIR})^{b} \tag{6}$$

$$\mathrm{SPM_{min(E)}} = a\, R_{rs}(\lambda_{NIR})^{b} \tag{7}$$

where the subscripts “org”, “min”, and “min (E)” indicate organic-rich, mineral-rich, and extremely mineral-rich water types, respectively. The λ_{Red} is 670 nm and λ_{NIR} is 810 nm. The a, and b are the best-fit regression model coefficients obtained with field data for respective water types.

2.3 SPM algorithm and satellite-derived SPM validation

We used 50% of the in situ samples (*n*=153) from our assembled dataset from the Arctic Ocean, Terrebonne Bay, Atchafalaya Delta, and Gironde Estuary to develop the SPM algorithms (Table 1). The remaining 50% of the in situ samples from this dataset, along with all samples from other datasets that were independent of the algorithm development dataset, were used for the SPM algorithm validation. We also compared the performance of the proposed SPM algorithm with eight previous algorithms, including empirical, semi-analytical, and machine learning algorithms, which were proposed by Balasubramanian et al. (2020); Doxaran et al. (2002); Jiang et al. (2021); Miller and McKee (2004); Nechad et al. (2010); Novoa et al. (2017); Petus et al. (2010); Yu et al. (2019).

For satellite-derived SPM validation, we validated our SPM estimates from satellite observations using a satellite-in situ matchup dataset. First, we paired Landsat-derived SPM with concurrent field measurements of SPM and then compared these matchups. Specifically, we extracted the satellite-derived SPM from a precise 30m x 30m pixel that overlapped with the exact location of the in situ SPM water sample, ensuring accurate spatial alignment. We only used water samples within a ± 2 hour window of the satellite overpass (between 8:00 AM and 12:00 PM local time for Landsat). Large rivers have discharge patterns that vary over seasonal timescale with sediment concentration closely linked to discharge, which allows for matchup flexibility in timing of satellite-field observation matchups. In contrast, the highly dynamic nature of coastal sediments—affected by wind waves, runoff, tides, fluctuating water levels, and river discharge—requires precise timing for data collection to ensure accurate matchups. Additionally, pixels affected by cloud/haze, shadows, snow/ice, adjacency effects or bottom reflectance were also excluded from matchups. In total, we compiled 22 matchups of field SPM measurements with concurrent Landsat imagery to validate our SPM retrieval algorithm. The SPM ranged from 0.1 to 77 g/m^3 with POC/SPM of 0.02-0.2, covering a range from organic to mineral rich particle assemblages.

Due to the limitations of validating satellite-derived SPM with a small sample size of satellite-in situ matchups, we also used continuous time-series of in situ measurements of water turbidity to complement the SPM validation analysis. While the determination of in situ SPM requires collection of discrete water samples and subsequent laboratory measurements, in situ turbidity measurements are often available at high temporal resolution for many major river deltas through USGS field gauge stations. Turbidity is an optical property of water, and therefore not a perfect approximation of SPM, but the two parameters are generally well correlated for a given river system (McKeon et al. 2022; Minella et al. 2007). Specifically, we used a 90 m buffer zone to extract satellite-derived SPM from the location of the turbidity sensor, and we extracted concurrent turbidity measurements within ±5 minutes of the Landsat overpass (between 9:55 AM and 10:05 AM local time). We employed two methods to validate our results. First, we compared the seasonal trends between satellite-derived SPM and in situ turbidity measurements. Second, we compared satellite-derived SPM with concurrent turbidity measurements.

The coefficient of determination (R^2), root mean square error in log space (RMSE), and the median absolute percent error (MAPE) were used to assess the algorithm performance defined as:

$$R^2 = 1 - \frac{\sum_{i=1}^{n} (y_i - \hat{y}_i)^2}{\sum_{i=1}^{n} (y_i - \bar{y})^2} \quad (8)$$

$$\text{RMSE} = \sqrt{\frac{\sum_{i=1}^{n} \left(\log(\hat{y}_i + 1) - \log(y_i + 1)\right)^2}{n}} \quad (9)$$

$$\text{MAPE} = \text{median}\left(\left|\frac{y_i - \hat{y}_i}{y_i}\right|\right) \times 100\% \quad (10)$$

where $\hat{y}_i$ is the predicted value, y_i is the measured value, $\bar{y}$ is the mean of the measured values, n is the number of samples.

3. Results

3.1 POC/SPM estimation and water type classification using in situ dataset

To assess the classification of water types based on particle composition, we first demonstrate the estimation of POC/SPM from in situ measurements of $R_{rs}(\lambda)$ using the concurrent data for all samples with paired POC and SPM measurements. The best-fit algorithm coefficients for the POC/SPM estimation (Eq. 1-4) are shown in Table 3.

Table 3. Coefficients and performance metrics for POC/SPM algorithms and water type classification based on the analysis of in situ dataset

Algorithm	a	b	POC/SPM algorithm performance		Water type classification performance
			R^2	RMSE	Overall accuracy (%)
Eq. 1, *f(B)*	-1.280	-4.012	0.82	0.04	90.3
Eq. 2, *f(G)*	-0.973	-3.213	0.86	0.03	92.2
Eq. 3, *f(R)*	-0.516	-2.431	0.86	0.03	91.9
Eq. 4, *f(B,G,R)*	a_1=-0.727, a_2=0.398, a_3=-0.509	-3.147	0.91	0.02	92.2

Fig. 6 shows the predicted POC/SPM versus measured POC/SPM for four different algorithms. Overall, all algorithms provide a good estimation of POC/SPM. The one-band algorithm can produce reasonably good estimates of POC/SPM, for example R^2=0.86, RMSE=0.04, and MAPE= 29.1% for the green band algorithm. The three-bands algorithm provides the best estimation of POC/SPM with R^2=0.91, RMSE=0.02, and MAPE= 24.70%. We chose the green band algorithm to estimate POC/SPM and classify water types because it provides the highest overall classification accuracy (92.2%), similar to the three-bands algorithm (92.2%) while slightly outperforming the red band algorithm (91.9%), and the blue band algorithm (90.3%) (n = 259). This demonstrates that the green band algorithm is as effective as the multiband approach for water type classification while being simpler and more practical to implement.

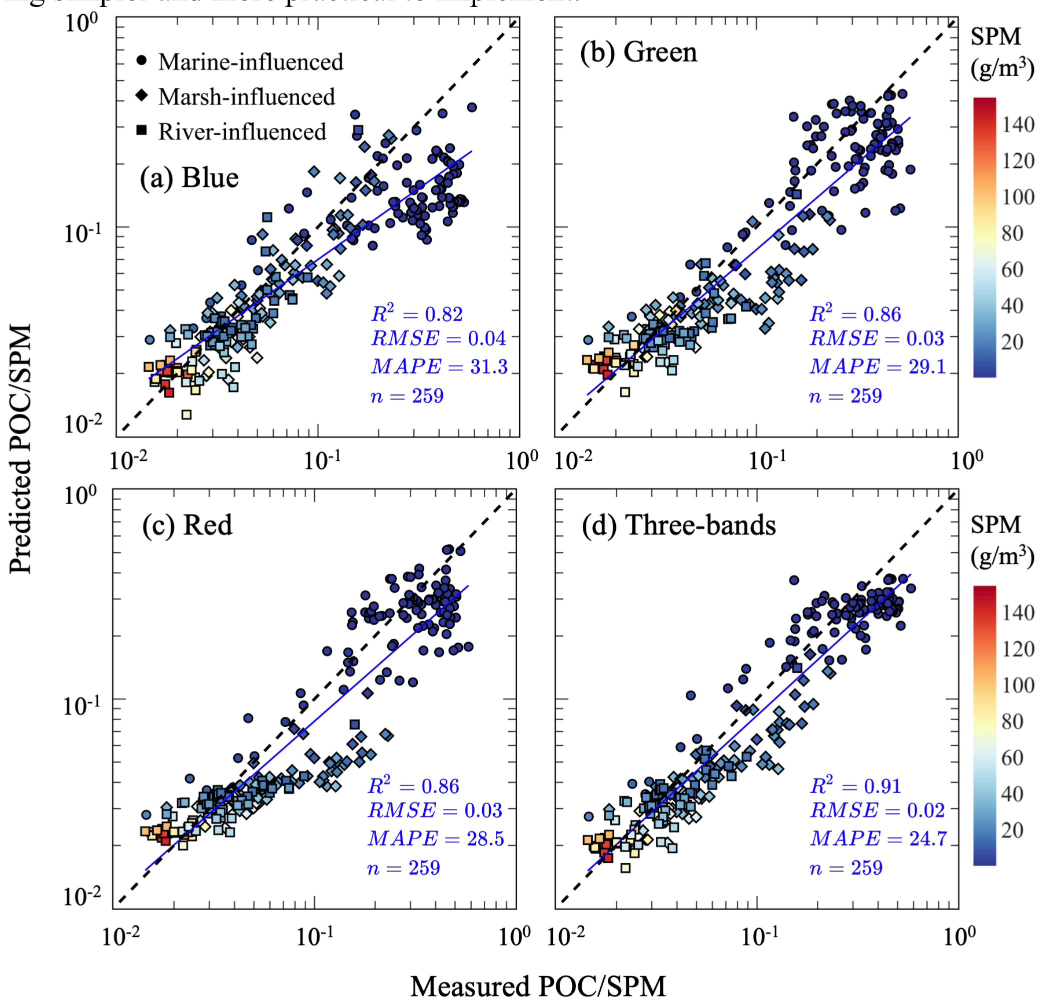

Figure 6. Algorithm-derived versus measured values of POC/SPM using different algorithms applied to the in situ dataset. (a) Blue band algorithm. (b) Green band algorithm. (c) Red band algorithm. (d) Three-bands algorithm.

In Stramski et al. (2023), water types were classified into three categories: the mineral-dominated class defined as having POC/SPM ≤ 0.12; the mixed class with POC/SPM between 0.12 and 0.28; and the organic-dominated class with POC/SPM ≥ 0.28. We adopted similar thresholds to Stramski et al. (2023). In our classification, water is categorized as extremely mineral-rich when POC/SPM < 0.02, mineral-rich when POC/SPM is between 0.02 and 0.12, and organic-rich when POC/SPM > 0.12 or $R_{rs}(670) < 0.01$ sr^{-1}. There are two main differences between these classification schemes: (i) we extended the previous classification of Stramski et al. (2023) by introducing an extremely mineral-rich category to account for very turbid and mineral-rich waters, such as those with SPM exceeding 1000 g/m^3 and the POC/SPM ratio below 0.02; (ii) we merged the mixed and organic-dominated categories from Stramski et al. (2023) into one organic-rich category. This adjustment was based on findings by Stramski et al. (2023) which showed no significant difference in the average spectral shape of $R_{rs}(\lambda)$ between the mixed and organic-dominated categories. For the organic-rich class, we used an additional criterion of $R_{rs}(670) < 0.01$ sr^{-1}, along with POC/SPM > 0.12, to better distinguish organic-rich particulate assemblages. This adjustment accounts for cases where POC/SPM is slightly below 0.12, but the lower $R_{rs}(670)$ suggests reduced scattering from mineral particles or increased phytoplankton absorption. Such cases were therefore grouped into the organic-rich water type.

3.2 SPM estimation for different water types using in situ dataset

3.2.1 Spectral characteristics of reflectance of organic and mineral-rich particulate matter

Fig. 7 shows example of in situ measurements of spectral $R_{rs}(\lambda)$ for organic-rich, mineral-rich, and extremely mineral-rich particle classes, exhibiting diverse shapes and magnitudes of $R_{rs}(\lambda)$ within and across particle composition classes. For the organic-rich class in Fig. 7a and 7b, the spectra typically show peaks in the blue or green regions. The contrast between $R_{rs}(670)$ and $R_{rs}(700)$ in Fig. 7b indicates a higher presence of phytoplankton in the water (Xue et al. 2015). For the mineral-rich class in Fig. 7c and 7d, the spectra generally peak in the green or red regions, showing overall higher levels of $R_{rs}(\lambda)$ due to increased backscattering by mineral particles. For the extremely mineral-rich particle class in Fig. 7e and 7f, the spectra typically peak in the green, red, or NIR regions.

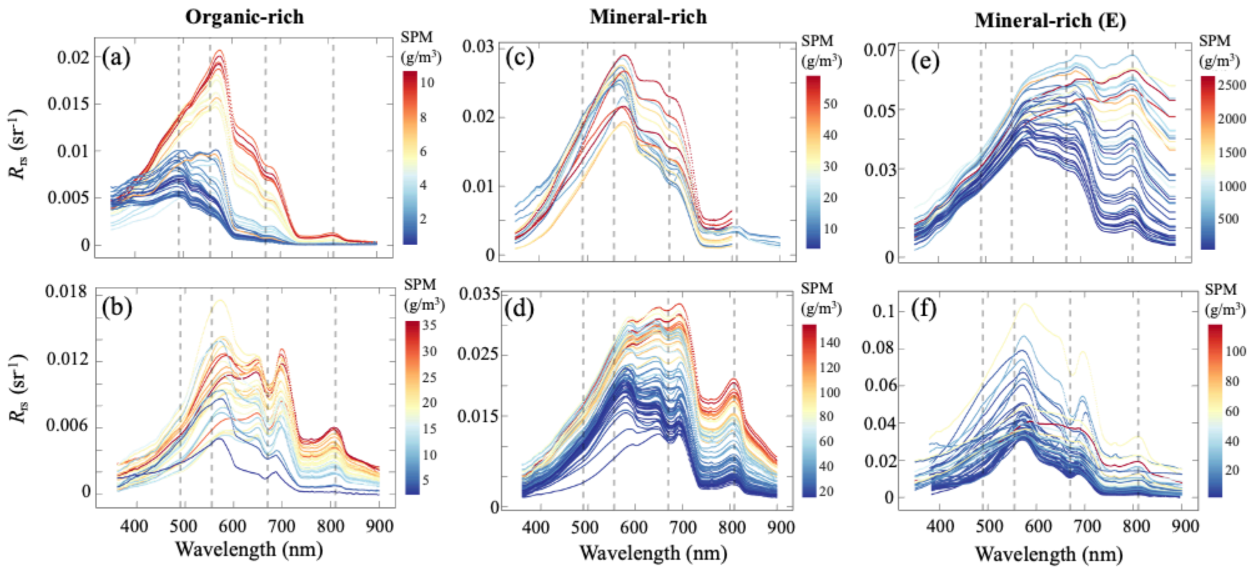

Figure 7. Example spectra of $R_{rs}(\lambda)$ from in situ observations for different particle composition classes where each spectral curve represents a single hyperspectral measurement. (a) Organic-rich particle class from Mekong River. (b) Organic-rich particle class from Terrebonne. (c) Mineral-rich particle class from English Channel and Hawke Bay. (d) Mineral-rich particle class from Terrebonne. (e) Extremely mineral-rich (E) particle class from Gironde River. (f) Extremely mineral-rich (E) particle class from English Channel. The vertical dashed lines correspond to wavelengths of 490 nm, 555 nm, 670 nm, and 810 nm.

Fig. 8a shows example $R_{rs}(\lambda)$ spectra for the three water types from in situ measurements. The reflectance characteristics of these water types exhibit distinct spectral trends and magnitudes. As the mineral fraction increases from the organic-rich to mineral-rich and extremely mineral-rich particle composition class, the dominant reflectance peak shifts to longer wavelengths. For the organic-rich class, the peak occurs in the green spectral region (~570 nm), while the mineral-rich and extremely mineral-rich classes show a peak at longer wavelengths (~700 nm). Additionally, the magnitude of $R_{rs}(\lambda)$ increases as the mineral fraction in SPM increases.

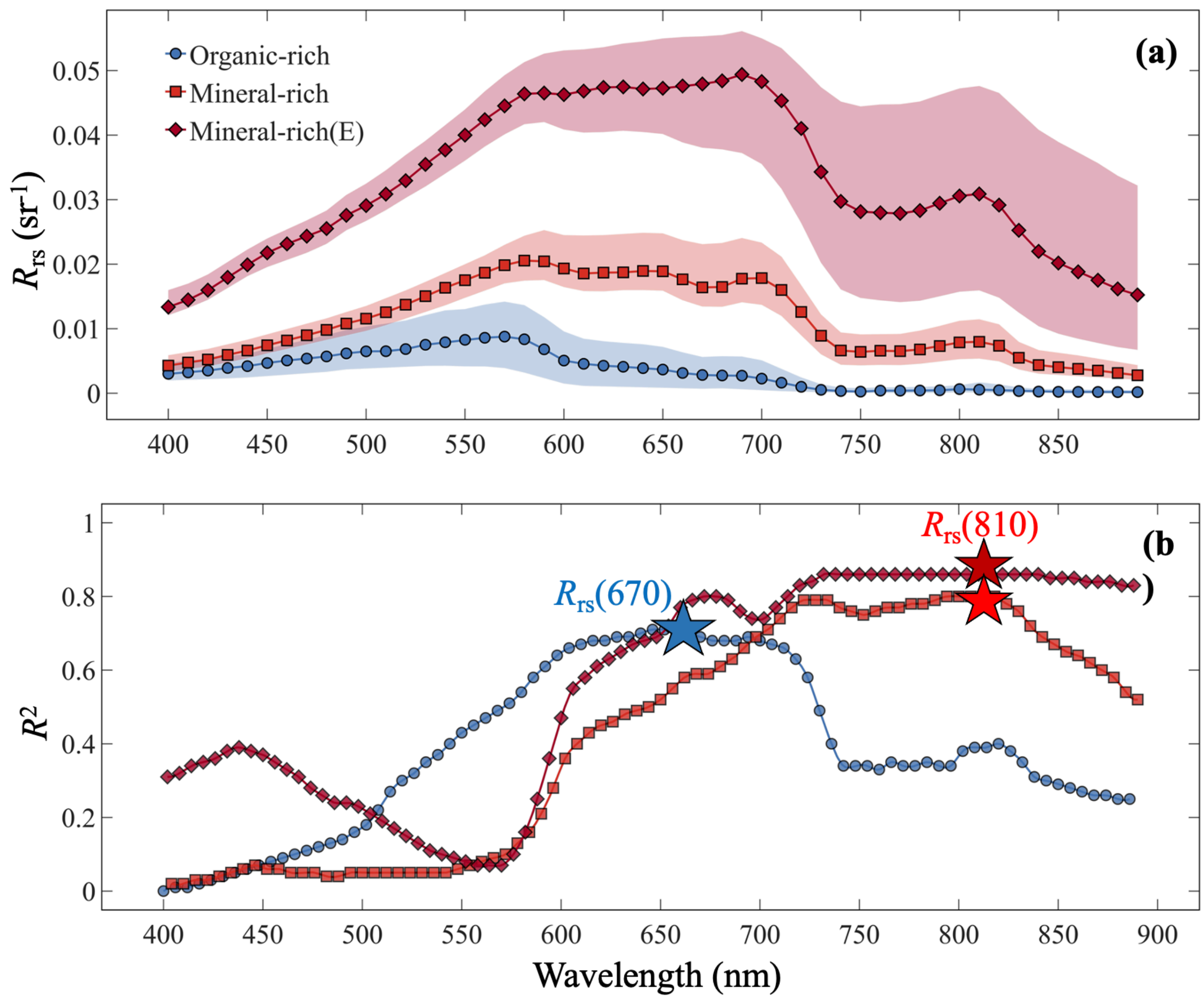

Figure 8. (a) Example $R_{rs}(\lambda)$ spectra for the three water types from in situ measurements. The shaded regions represent the interquartile range (IQR, 25th–75th percentile), while the solid line with circular markers indicates the median R_{rs} at each wavelength. Wavelengths are shown at 10 nm intervals from 400 nm to 890 nm for illustrative purposes. (b) The R^2 values of linear regression between log-transformed SPM and $R_{rs}(\lambda)$ from 400 to 890 nm for three particle composition classes. The blue and red stars mark the optimal wavelengths for organic-rich waters (~670 nm) and mineral-rich and extremely mineral-rich (E) waters (~810 nm), respectively.

3.2.2 Optimal wavelength for SPM estimation

To determine which wavelength of $R_{rs}(\lambda)$ can serve as the best predictor of SPM for different water types, we fitted a linear regression between log-transformed values of field measurements of SPM and $R_{rs}(\lambda)$ in the spectral range 400–890 nm. Fig. 8b shows the determination coefficient, R^2, for estimating SPM from $R_{rs}(\lambda)$, across different wavelengths for the three water types. The coefficient R^2 exhibits significant variation across the spectral range and displays unique spectral behavior for each water type. For the organic-rich particle class, R^2 was highest in the red region with a peak around $R_{rs}(670)$. For both the mineral-rich and extremely mineral-rich particle classes, R^2 was highest in the near-infrared (NIR) region with a peak around $R_{rs}(810)$. Although $R_{rs}(730)$ also shows high R^2 values for the mineral-rich and extremely mineral-rich classes, this band is unavailable on most land observation satellites. Overall, R_{rs} at visible bands can predict SPM for organic-rich particle assemblages well, whereas the NIR bands can predict mineral-rich particle assemblages well. Fig. 9 shows the relationships between SPM and optimized $R_{rs}(670)$ or $R_{rs}(810)$ for the three water types. It is clear that $R_{rs}(670)$ can better predict SPM for organic-rich class, whereas $R_{rs}(810)$ can better predict SPM for mineral-rich and extremely mineral-rich classes.

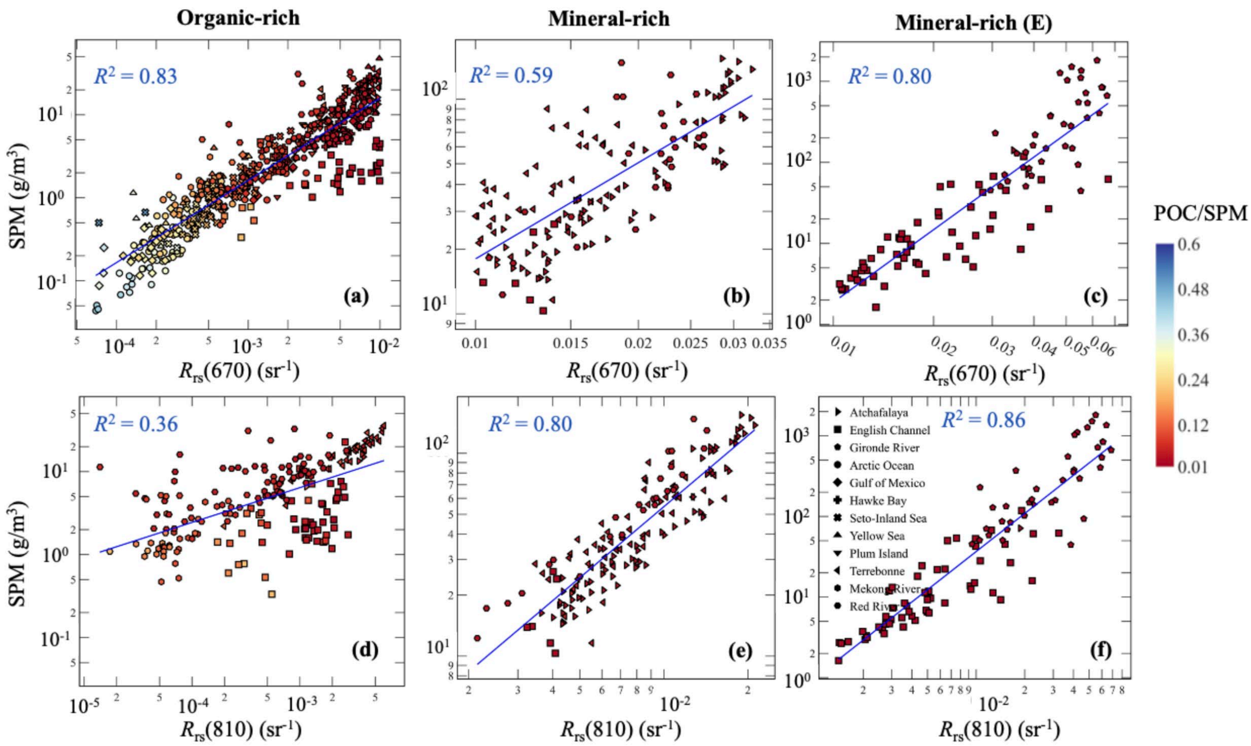

Figure 9. Measured SPM versus in situ R_{rs} (Red = 670 nm and NIR = 810 nm) for the three particle composition classes. (a) SPM vs. $R_{rs}(670)$ for organic-rich particle class. (b) SPM vs. $R_{rs}(670)$ for mineral-rich class. (c) SPM vs. $R_{rs}(670)$ for extremely mineral-rich class. (d) SPM vs. $R_{rs}(810)$ for organic-rich class. (e) SPM vs. $R_{rs}(810)$ for mineral-rich class. (f) SPM vs. $R_{rs}(810)$ for extremely mineral-rich class.

3.2.3 Particle composition-specific SPM algorithms

Based on the variability of the algorithm performance using different wavelengths for different water types illustrated in Fig. 8 and 9, we selected the most appropriate spectral band to predict SPM from $R_{rs}(\lambda)$ for each water type. Accordingly, we derived the following best-fit algorithmic formulas for each water type (Eq. 5-7) using in situ spectral measurements (see Table 1 foir summary of data). The coefficients for particle composition-specific SPM algorithms are presented in Table 4 and the corresponding plots are shown in Fig. S2. The organic-rich specific algorithm uses the red band and shows a near linear relationship between the red band reflectance and SPM with a relatively small slope (a=1992.2, b=1.027). In contrast, the mineral-rich specific algorithms, both using the near-infrared (NIR) band, exhibit stronger non-linear relationships. The mineral-rich specific algorithm has a steeper increase in SPM as a function of NIR reflectance (a=12662.7, *b*=1.157) than the organic-rich specific algorithm. The extremely mineral-rich (E) specific algorithm shows the most rapid increase in SPM (*a*=50556.7, *b*=1.371).

Table 4. Coefficients of particle composition-specific SPM algorithms (Eq. 5-7)

Algorithm	*a*	*b*
Organic-rich	1992.2	1.027
Mineral-rich	12662.7	1.157
Mineral-rich (E)	50556.7	1.371

3.3 Validation of SPM algorithm

3.3.1 SPM algorithm validation using in situ reflectance spectra and SPM

Fig. 10 shows the algorithm-derived versus measured values of SPM for all 12 field experimental sites (Table 1) using particle composition-specific algorithms described by Eq. 5-7. All samples included in this illustration are independent from the algorithm development dataset. The algorithms produce reasonably good estimates of SPM across diverse coastal environments, with the mean values of R^2 of 0.77, MAPE of 32.9%, and RMSE of 0.16. The performance of the algorithms varied slightly between sites, which may reflect regional differences in particle composition, particle size distribution, absorption by colored dissolved organic matter, and environmental factors, such as sky conditions and sea surface boundary conditions.

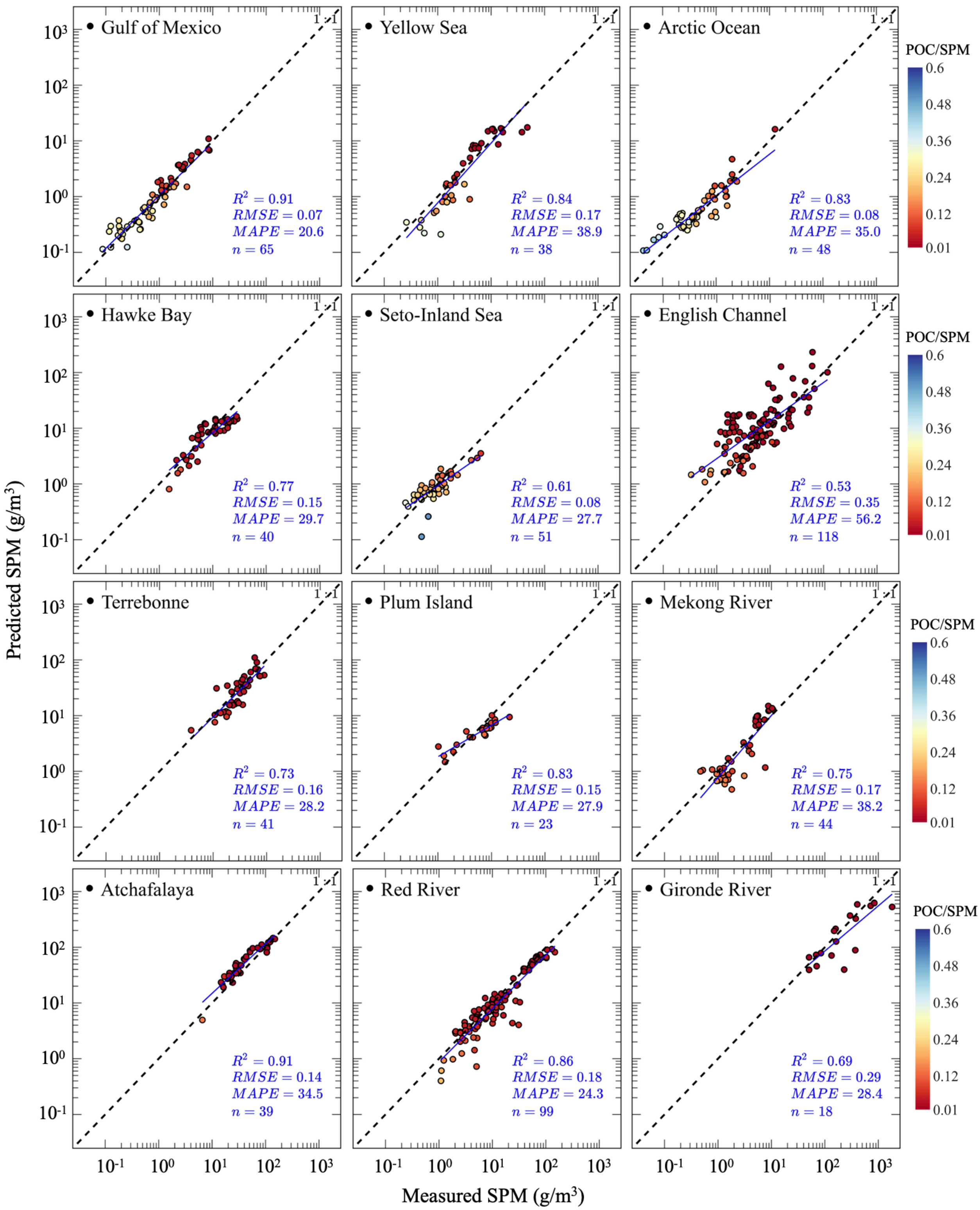

Figure 10. Algorithm-derived versus measured values of SPM using our particle composition-specific SPM retrieval algorithm with data points color coded according to the predicted POC/SPM values obtained from our green band POC/SPM algorithm. The SPM values were estimated from

in situ R_{rs} measurements at a single band for different sites according to the water type classification in terms of particle composition parameter POC/SPM. (a) Gulf of Mexico, (b) Yellow Sea, (c) Arctic Ocean, (d) Hawke Bay, (e) Seto-Inland Sea, (f) English Channel, (g) Terrebonne, (h) Plum Island, (i) Mekong River, (j) Atchafalaya, (k) Red River, and (l) Gironde River. The sample size is slightly different from that in Table 1 because the mineral-rich samples at some sites lack in situ measurement of $R_{rs}(810)$.

3.3.2 Comparison with previous SPM algorithms

We assessed the performance of the proposed SPM retrieval algorithm in comparison to eight previously published algorithms (Table 5). These previous publications include empirical, semi-analytical, and machine learning algorithms as outlined in Table S1. The primary goal of this comparison is to provide insights into the performance of different algorithms across various water types and to highlight the development of SPM algorithms over the past two decades. Rather than determining which algorithm is the best, this comparison aims to present the range of algorithm performance. An attempt to identify the best algorithm would be challenging and likely difficult to justify mainly for two reasons: (i) each algorithm is designed with specific objectives utilizing different spectral bands and calibrated with different datasets; (ii) the availability of validation data varies for each algorithmic method depending on the spectral bands required in the method. For instance, some algorithms including Doxaran et al. (2002), Novoa et al. (2017), Yu et al. (2019), Balasubramanian et al. (2020), and Jiang et al. (2021) require R_{rs} in the NIR region, which is not always available for in situ R_{rs} measurement due to instrumental and processing constraints. In addition, the removal of negative values of SPM predictions also affects the number of validation data. For instance, 258 out of 816 samples were predicted to have negative SPM values in the study of Miller and McKee (2004). This could also occur when calculating the absorption coefficient and backscattering coefficient using semi-analytical algorithms, such as those by Jiang et al. (2021) and Balasubramanian et al. (2020).

Table 5. Comparison of algorithm performance metrics for the proposed SPM algorithm with those from the literature.

Algorithm	R^2	RMSE	MAPE	*n*
Doxaran et al., 2002	0.61	0.52	89.5	456
Miller and McKee, 2004	0.53	0.43	63.0	540
Nechad et al., 2010	0.82	0.36	54.4	718
Petus et al., 2010	0.81	0.33	53.0	718
Novoa et al., 2017	0.83	0.26	40.4	716
Yu et al., 2019	0.76	0.30	41.6	459
Balasubramanian et al., 2020	0.86	0.27	39.6	718
Jiang et al., 2021	0.76	0.28	35.0	595
This study	0.91	0.20	30.5	770

The performance of each algorithm is shown in scatter plots of algorithm-derived versus measured values of SPM (Fig. 11). Each algorithm exhibits some limitations. For example, Doxaran et al. (2002) cannot reliably estimate relatively low values of SPM as their algorithm is designed primarily for highly turbid waters. The algorithms of Miller and McKee (2004), Nechad et al. (2010), and Petus et al. (2010) have difficulty with the estimation of both low and high SPM levels. The errors in low SPM waters were likely due to the low signal-to-noise ratio of red reflectance in clear waters and inadequate algorithm calibration for clear waters, while the errors in high SPM waters were primarily caused by the saturation of red reflectance. This highlights a fundamental limitation of SPM retrieval algorithms that are based solely on visible spectral bands. The algorithms developed by Novoa et al. (2017) and Yu et al. (2019) perform well in predicting intermediate to high SPM but have difficulty with low SPM, likely due to the lack of organic-rich water samples (such as those from the Arctic Ocean) in the dataset used to calibrate the algorithm. The SOLID algorithm by Balasubramanian et al. (2020) perform well in predicting low SPM but displays larger errors at intermediate and high SPM. The Jiang et al. (2021) algorithm shows strong performance in predicting intermediate values of SPM but is less effective at low and high particle concentrations. These two algorithms were designed for diverse aquatic environments ranging from open coastal areas to inland waters, making them more suitable for global SPM estimation. However, it appears they are unlikely to effectively capture the variability in particulate composition within coastal waters. Our proposed algorithm produces reasonably accurate estimates across the very wide range of SPM typically observed in coastal waters. Notably, our algorithm achieved the highest R^2=0.91 among the compared algorithms (0.53-0.86 range), the smallest RMSE value of 0.20 (0.26-0.52 range for other algorithms), and smallest MAPE value of 30.5% (35.0%–89.5% for other algorithms). Moreover, our approach utilizes only three spectral bands for water type classification and SPM estimation, which are available on most land observation satellites, enhancing its applicability with this type of satellite sensors.

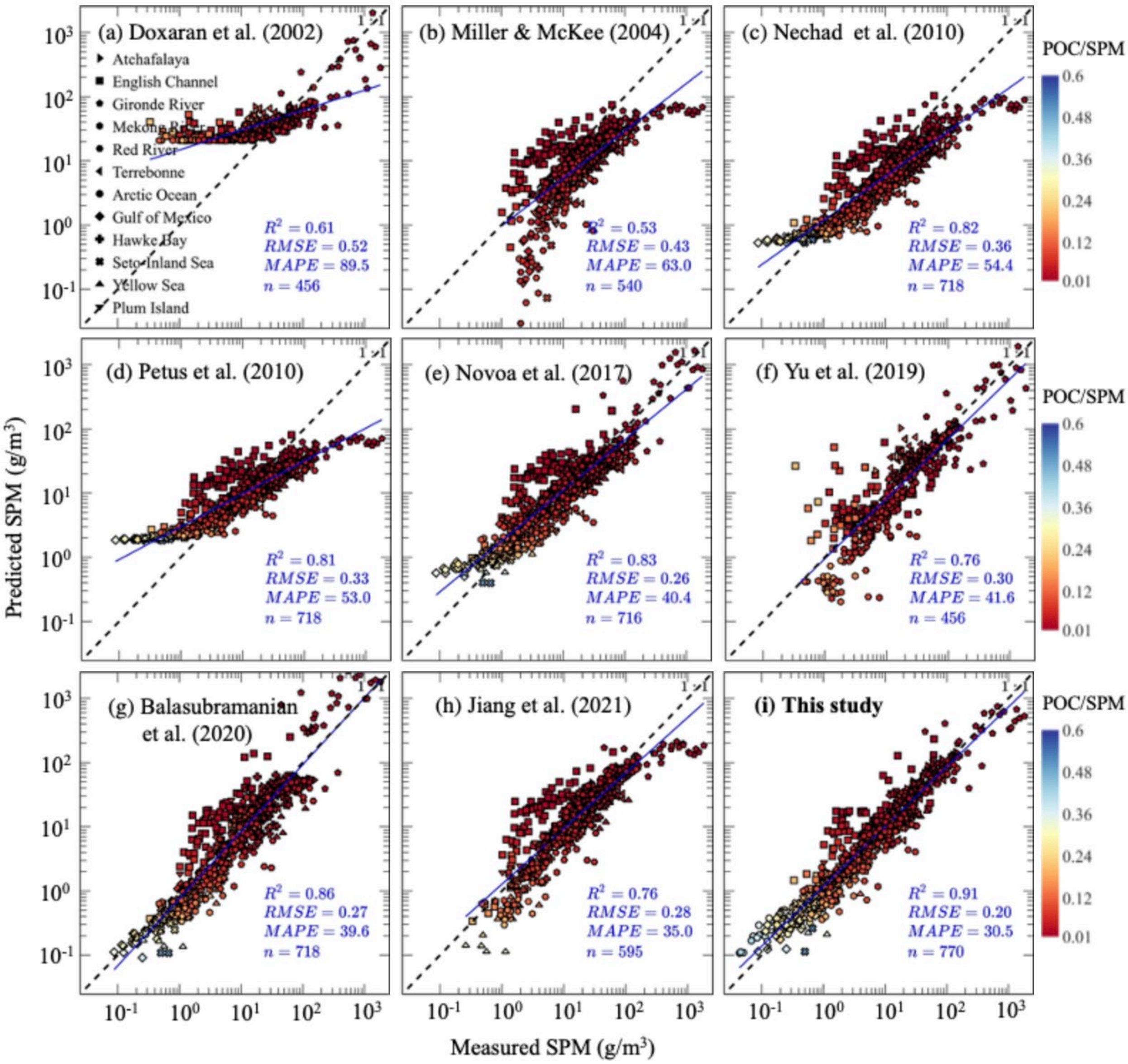

Figure 11. Comparison of algorithm-derived SPM with in situ measurements of SPM. The estimated SPM values were obtained from in situ-measured $R_{rs}(\lambda)$ using different SPM algorithms. (a) Doxaran et al. (2002). (b) Miller and McKee (2004). (c) Nechad et al. (2010). (d) Petus et al. (2010). (e) Novoa et al. (2017). (f) Yu et al. (2019). (g) Balasubramanian et al. (2020). (h) Jiang et al. (2021). (i) This study. All points are color coded according to the predicted POC/SPM from our green band POC/SPM algorithm.

3.4 Validation of satellite-derived SPM

3.4.1 Landsat radiometric correction

To apply the proposed particle composition-specific SPM algorithms to Landsat images, we used empirical line method to correct the Landsat Surface Reflectance (SR) image by removing the reflection of skylight at the air-water interface to align the SR values with in situ-measured remote-sensing reflectance $R_{rs}(\lambda)$. We plotted the in situ-measured $R_{rs}(\lambda)$ versus Landsat SR for four major spectral bands of Landsat (Fig. S3). Overall, there was good agreement between the measured $R_{rs}(\lambda)$ and the Landsat SR, indicating that the Landsat Level-2 Surface Reflectance Science Product is retrieved relatively well from the applied atmospheric correction procedure. This is also supported by the study of Page et al. (2019), which shows that the spectral shape and magnitude of SR product are very similar to those produced by other atmospheric correction methods designed for ocean color remote sensing. However, residuals still exist due to skylight reflection at the water surface and other errors. We applied the empirical line method to directly correct the Landsat SR to align with $R_{rs}(\lambda)$ measured in situ at the specific wavelengths, including $R_{rs}(490)$, $R_{rs}(555)$, $R_{rs}(670)$, and $R_{rs}(810)$.

3.4.2 Validation of SPM retrievals using satellite-in situ matchups

Fig. 12 shows the comparison between Landsat-derived SPM and in situ-measured SPM using the proposed SPM algorithms. When applied to Landsat imagery, the proposed algorithm produces SPM that agrees reasonably well with match-up measurements of SPM across diverse water bodies ranging from organic-rich to mineral-rich water types with R^2 of 0.93, MAPE of 22%, RMSE of 7.8 g/m^3. However, validating SPM using satellite-in situ matchups presents challenges, primarily due to the small sample size. The highly dynamic nature of coastal sediments—impacted by wind waves, runoff, tides, fluctuating water levels, and river discharge—requires precise timing for data collection to secure accurate matchups. To address these limitations, we also used time-series data of in situ measurements of water turbidity to enhance our SPM validation analysis, as detailed below in §3.4.3.

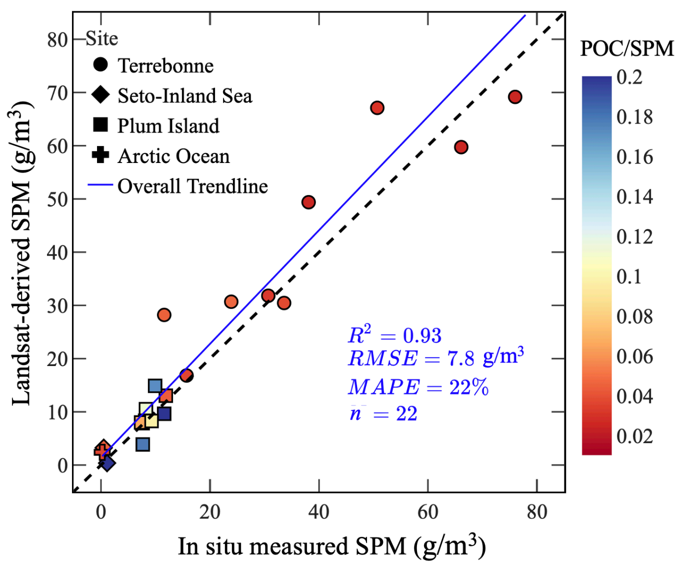

Figure 12. Comparison of Landsat-derived SPM and in situ measured SPM using the proposed SPM algorithm. The RMSE value was calculated using the original data, i.e., not in the log space.

3.4.3 Validation using water turbidity measurements

The US Geological Survey (USGS) maintains a network of stream gauges providing continuous water turbidity measurements for many major US estuaries, allowing for an alternative assessment of the satellite SPM retrievals from the proposed SPM algorithm. Fig. 13 shows the comparison of in situ-measured turbidity and satellite-derived SPM for selected sites including East Coast, USA: Connecticut River, Gulf of Mexico, USA: Atchafalaya, West Coast, USA: San Francisco

Bay, Pacific Northwest, Canada: Taku River, and East Coast, USA: Back River. The left panel of Fig. 13 shows the time series of in situ turbidity measurement and satellite estimate of SPM. The right panel of Fig. 13 depicts a scatter plot comparing satellite-derived SPM matched with in situ turbidity measurements. The first three sites illustrate the seasonal variability of SPM and turbidity, while the last two sites illustrate the annual variability.

Satellite retrievals of SPM effectively capture the seasonal variations in the Connecticut River Mouth and Atchafalaya but provide less comprehensive data for San Francisco Bay. More specifically, in the Connecticut River Mouth, the satellite data capture three major turbidity peaks in March, July, and December. The estimated SPM strongly correlates with observed turbidity ($R^2 = 0.81$, $p < 0.001$). At the Atchafalaya site, satellite observations reflect the seasonal turbidity pattern with high SPM in spring and low SPM in summer, and the estimated SPM also shows a strong correlation with observed turbidity ($R^2 = 0.74$, $p < 0.001$). In San Francisco Bay, although there are fewer observations throughout the year and seasonal variability is not well captured, the estimated SPM still correlates significantly with observed turbidity ($R^2 = 0.76$, $p < 0.001$).

In the Taku River, satellite observations capture the annual turbidity changes with estimated SPM showing a strong correlation with observed turbidity ($R^2 = 0.65$, $p < 0.001$). In Back River, there is no distinct annual turbidity pattern, but a general declining trend from 2000 to 2005 is apparent in both in situ and satellite observations. The correlation between estimated SPM and observed turbidity is relatively weaker compared to other sites but remains significant ($R^2 = 0.45$, p < 0.001).

The satellite-derived SPM does not directly represent turbidity measurements due to site-specific variations in the relationship between these two variables and the discrepancies are influenced by factors such as particle composition and size distribution driven by different sediment sources and processes over various time scales. Nonetheless, all validation sites exhibit a positive and significant correlation between satellite-derived SPM and in situ turbidity measurements.

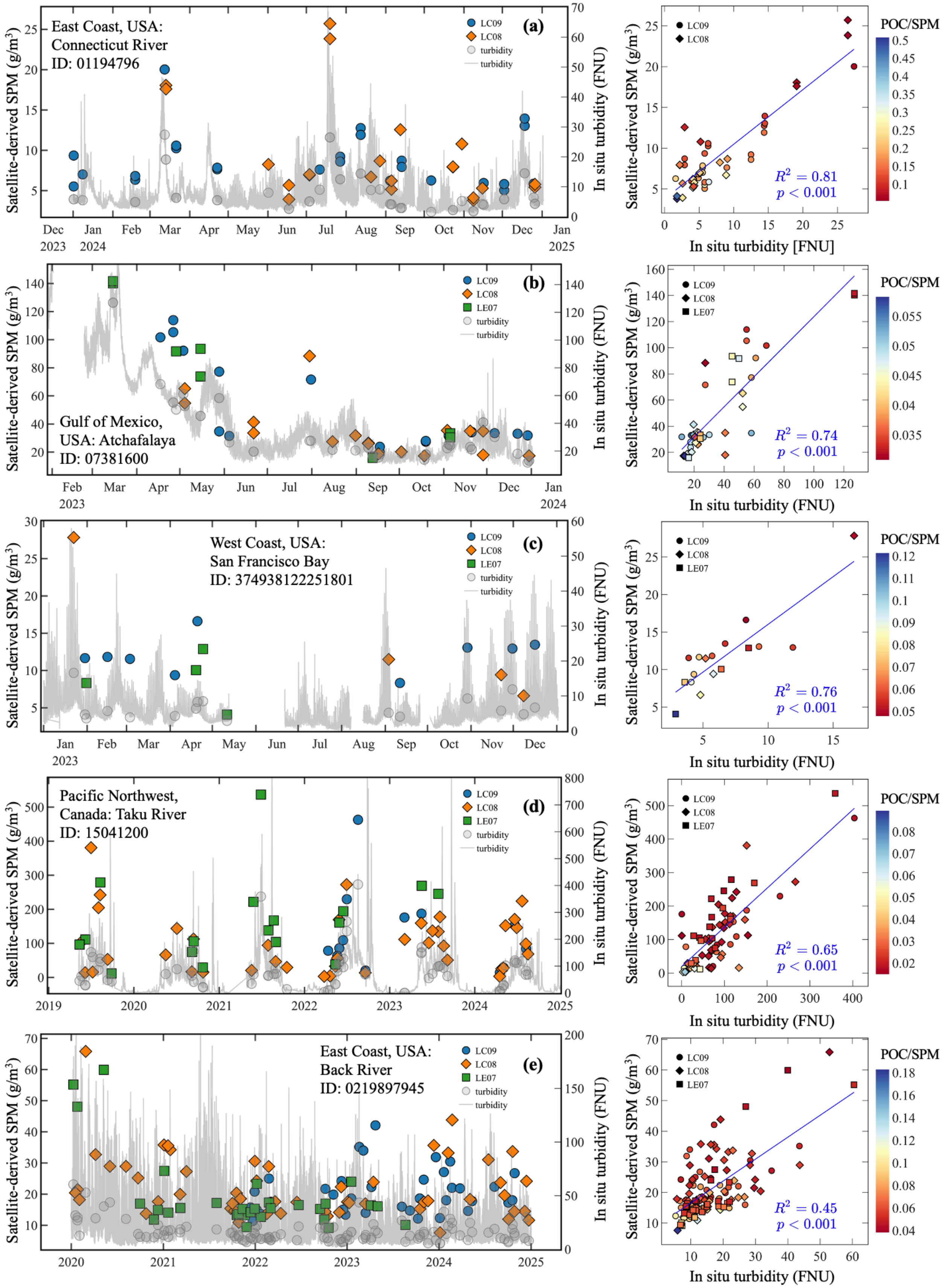

(a)
East Coast, USA:
Connecticut River
ID: 01194796
LC09
LC08
turbidity
turbidity
Satellite-derived SPM (g/m^3)
In situ turbidity (FNU)
Dec 2023
Jan 2024
Feb
Mar
Apr
May
Jun
Jul
Aug
Sep
Oct
Nov
Dec
Jan 2025
POC/SPM
$R^2 = 0.81$
$p < 0.001$
In situ turbidity [FNU]
(b)
Gulf of Mexico,
USA: Atchafalaya
ID: 07381600
LC09
LC08
LE07
turbidity
turbidity
Feb 2023
Jan 2024
POC/SPM
$R^2 = 0.74$
$p < 0.001$
In situ turbidity (FNU)
(c)
West Coast, USA:
San Francisco Bay
ID: 374938122251801
LC09
LC08
LE07
turbidity
turbidity
Jan 2023
POC/SPM
$R^2 = 0.76$
$p < 0.001$
In situ turbidity (FNU)
(d)
Pacific Northwest,
Canada: Taku River
ID: 15041200
LC09
LC08
LE07
turbidity
turbidity
2019
2020
2021
2022
2023
2024
2025
POC/SPM
$R^2 = 0.65$
$p < 0.001$
In situ turbidity (FNU)
(e)
East Coast, USA:
Back River
ID: 0219897945
LC09
LC08
LE07
turbidity
turbidity
2020
2021
2022
2023
2024
2025
POC/SPM
$R^2 = 0.45$
$p < 0.001$
In situ turbidity (FNU)

Figure 13. Comparison of in situ-measured water turbidity (Formazin Nephelometric Units, FNU) and satellite-derived SPM in several selected sites: (a) East Coast, USA: Connecticut River, (b) Gulf of Mexico, USA: Atchafalaya, (c) West Coast, USA: San Francisco Bay, (d) Pacific Northwest, Canada: Taku River, and (e) East Coast, USA: Back River. The left panel shows the time series of in situ turbidity measurement (secondary y axis) and satellite estimated SPM from matchup (primary y axis). The right panel shows scatter plot of these matchup data of satellite estimated SPM and in situ turbidity measurement with data points color-coded according to the satellite-derived POC/SPM ratio using our green band POC/SPM algorithm. The LC09, LC08, and LE07 represent Landsat 9, 8 and 7, respectively.

3.5 SPM mapping products

To enhance the exploration and visualization of coastal SPM dynamics, we developed an interactive web tool that provides high-spatial resolution satellite-based mapping of SPM globally. The tool allows users to create their own maps of SPM in coastal waters and explore both seasonal variations and long-term changes in SPM. It is publicly available and can be accessed at https://tssmapping.projects.earthengine.app/view/sscmap.

3.5.1 High spatial resolution patterns of satellite-derived SPM

To demonstrate the proposed algorithm for satellite-based mapping of spatial distributions of SPM, we selected two representative Landsat images, one from the northeast US, a high wave energy, organic-rich coastal marine environment, and the other from Louisiana (USA), a mineral-rich, low wave energy near-shore environment (Fig. 14). The high-spatial resolution SPM map in Fig. 14a clearly illustrates sediment plumes along the northeast coast. In this region, SPM is generally low due to the absence of major river mouths, which results in a limited riverine sediment supply. Instead, coastal geomorphic features, such as tidal marshes, primarily rely on nearshore glacial sediments that are mobilized by storms and high wave activity offshore (Baranes et al. 2022; Yellen et al. 2023). In contrast, the Mississippi River coast, as shown in Fig. 14b, exhibits higher SPM. In this region, SPM is largely associated with sediment discharge from the Atchafalaya River, one of the Mississippi River's main distributary branches. The high spatial-resolution SPM map in Fig. 14b also captures streaklines which are formed by a series of fluid parcels originating at the outlet of the Atchafalaya River (Salter et al. 2022).

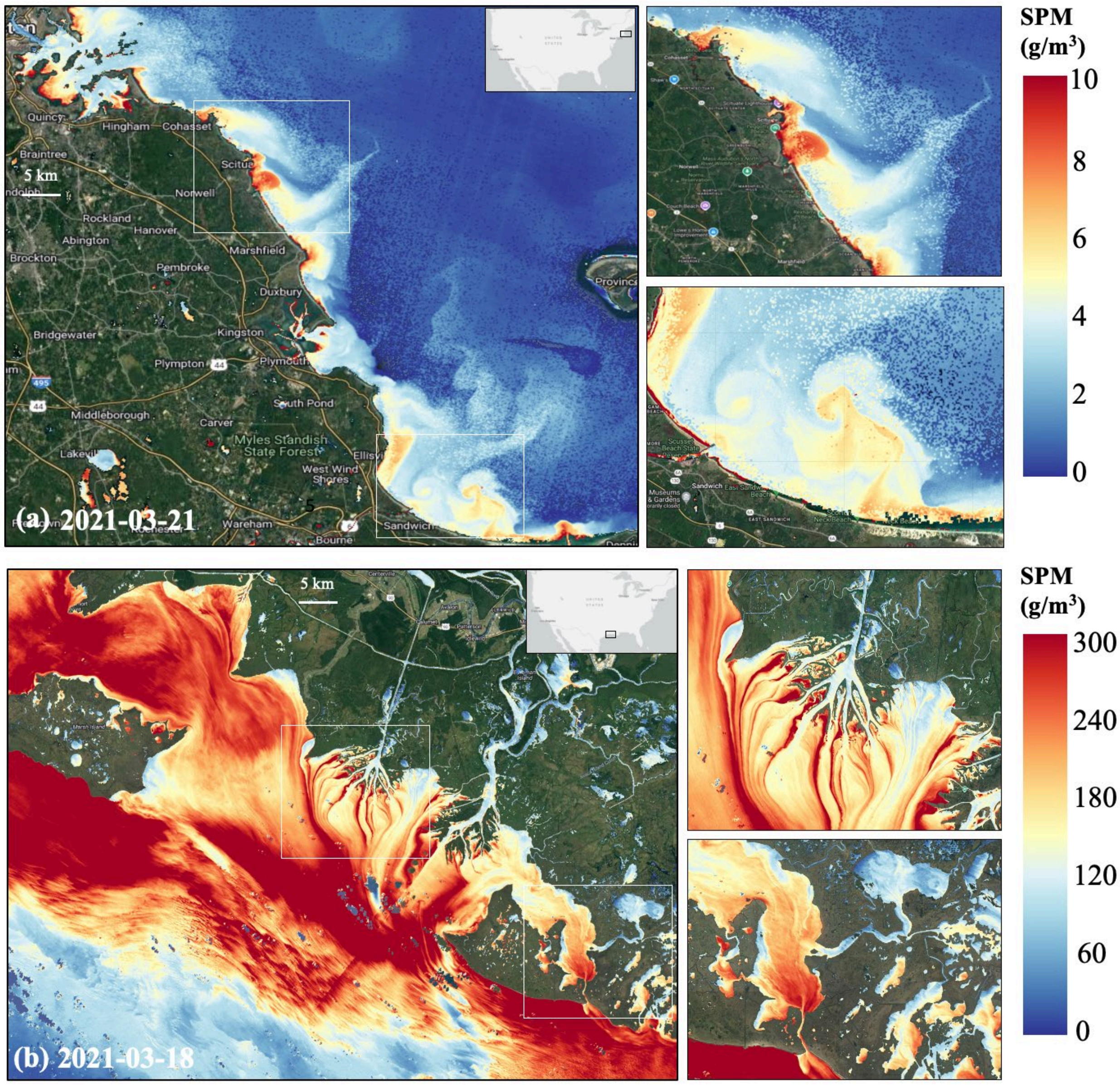

Figure 14. Spatial pattern of Landsat 8-derived SPM. (a) Northeast US coast (March 21, 2021). (b) Mississippi River Delta (March 18, 2021). The insets on right hand side provide zoomed-in views of specific areas, illustrating finer details of the SPM pattern.

3.5.2 Seasonal variations of satellite-derived SPM

We used the entire Landsat 5-9 catalog (1984-2024) to examine how seasonal trends of SPM vary between three representative coastal areas in the US. In San Francisco Bay (Fig. 15a), SPM shows notable seasonal variations with elevated SPM during spring and summer, contrasting sharply with lower values in autumn and winter. In the northeastern US (Fig. 15b), SPM levels increase during winter and spring, and decrease during summer and autumn. In the Atchafalaya Delta (Fig. 15c), SPM is lower in autumn but higher during winter, spring, and summer, peaking in May, consistent with the timing of monthly peak discharge from the Mississippi River (Androulidakis and

Kourafalou 2013). These results together demonstrate that this new Landsat-derived SPM product is capable of capturing the seasonal variability of SPM in diverse coastal marine environments.

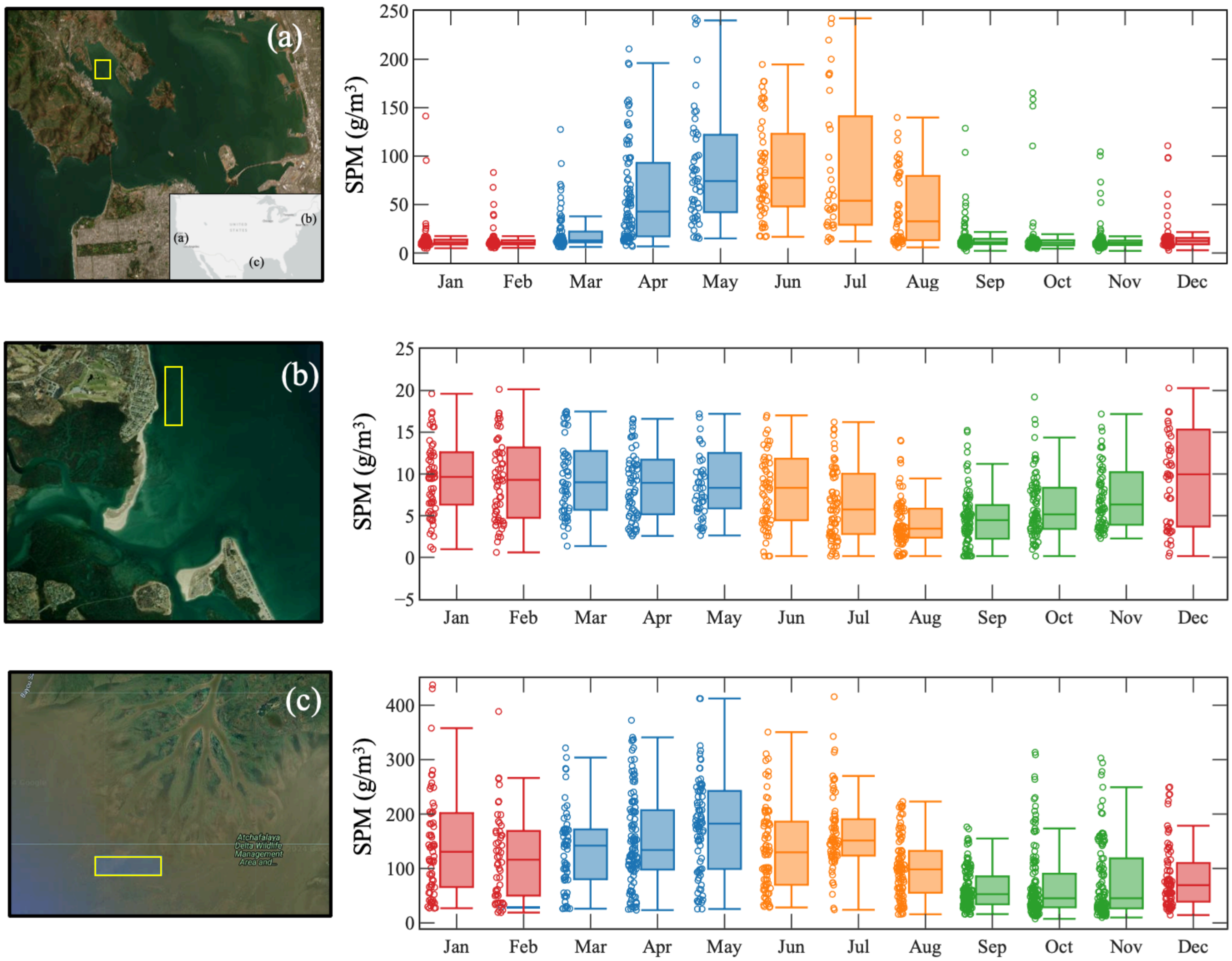

Figure 15. Seasonal variability of SPM over past 4 decades derived from Landsat 5, 7, 8, 9 over the period 1984-2024 for several coastal regions. The solid centerline refers to the median SPM. (a) San Francisco Bay. (b) North South River in northeastern US. (c) Atchafalaya Delta.

3.5.3 Satellite-derived SPM variability over decadal scales

To demonstrate SPM dynamics over the past four decades, we calculated Sen's slope (Sen 1968) using five-year binned SPM data derived from Landsat observations between 1984 and 2023 for two selected coastal sites (Fig. 16). The rationale of using five-year binned SPM is further detailed in §4.3. Fig. 16a shows a contrasting increase in SPM in Lake Pontchartrain and a decrease in the Atchafalaya River and its delta. In Fig. 16c, a contrasting result is also visible with an increase in SPM in the upper region of Blackwater and a decrease in Fishing Bay and the areas in Blackwater that receive sediment from Fishing Bay via connected channels. Fig. 16b and d show two contrasting SPM time series, one with a decrease and one with an increase. These results demonstrate the ability of the new Landsat-derived SPM product to capture SPM dynamics in coastal marine environments over a long multidecadal period.

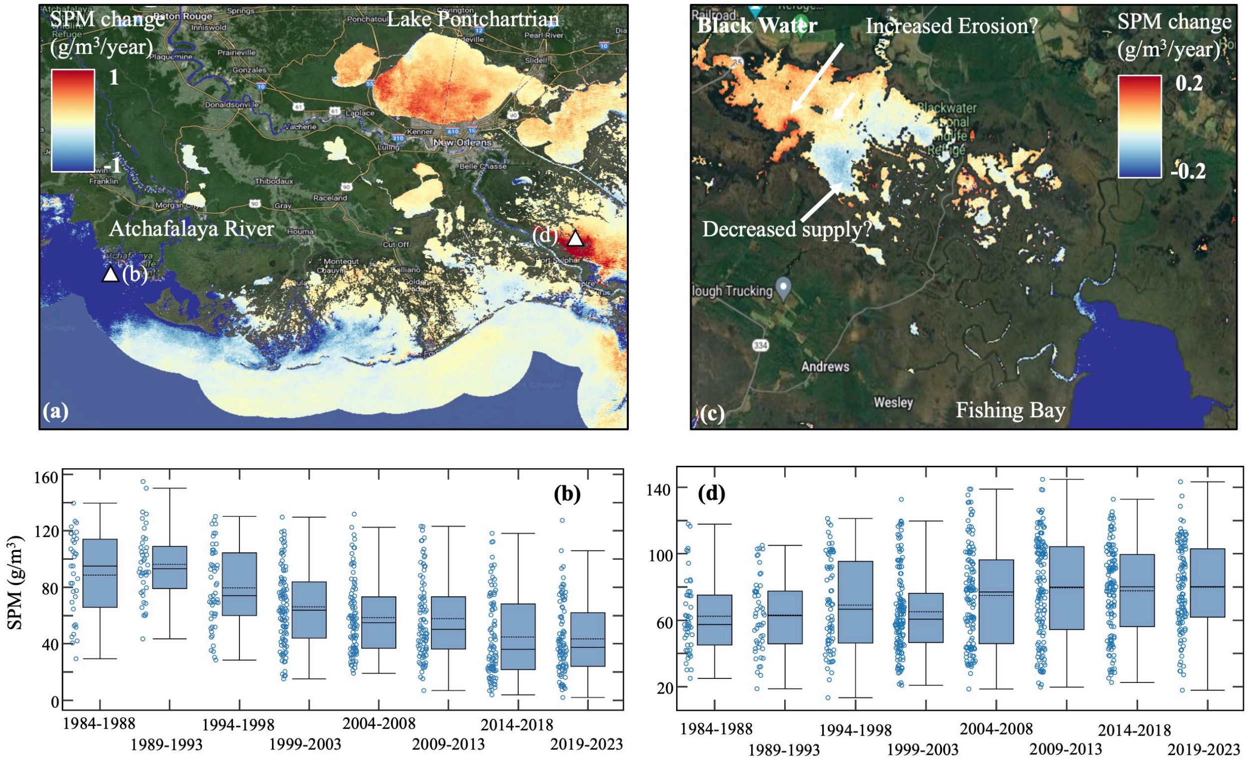

Figure 16. Sen's slope (g/m^3/year) of Landsat-derived SPM over the past four decades (1984 to 2023) (a) Atchafalaya River and Lake Pontchartrain. (c) Blackwater and Fishing Bay. Panels (b) and (d) display box plots of SPM at five-year intervals, illustrating temporal trends in SPM levels. The location of (b) and (d) are marked in the map (a).

4 Discussion

4.1 The rationale of particle composition-specific SPM algorithms

The classification of water types based on particle composition significantly enhances the accuracy of SPM estimation. By categorizing water bodies into distinct water type classes, such as organic-rich, mineral-rich, and extremely mineral-rich composition of suspended particulate matter, and using different particle composition-specific algorithmic formulas for SPM estimation from remote-sensing reflectance at different spectral bands, $R_{rs}(\lambda)$, the proposed algorithm effectively accounts for varying optical properties across diverse water types in optically-complex coastal environments.

This particle composition-based classification of water types is especially useful because the optical properties of natural waters are influenced not only by the concentration of suspended particles (i.e., SPM) but also by the composition and size distribution of particulate matter (Jerlov 1976; Jonasz and Fournier 2007). Specifically, for a given SPM, $R_{rs}(\lambda)$ tends to increase across the major portion of the visible spectrum as the POC/SPM ratio decreases, and this trend is clearly observed within the range of relatively high SPM typical of many coastal environments (Fig. 5). This result indicates that mineral-rich waters, which have a low POC/SPM ratio potentially accompanied by a higher proportion of smaller-sized particles, tend to exhibit higher $R_{rs}(\lambda)$ (Stramski et al. 2023). This is because an increased proportion of inorganic particles in SPM raises the average index of refraction of bulk particulate matter and a greater proportion of smaller particles increases the slope of particle size distribution (PSD), both of which either enhance the magnitude of backscattering or a proportion of backscattering in the total particulate scattering, which generally act to increase $R_{rs}(\lambda)$ (Bhargava and Mariam 1991; Boss et al. 2004; Reynolds et al. 2016; Twardowski et al. 2001). The effects of particle composition on $R_{rs}(\lambda)$ suggest that a single predictive model generally cannot reliably estimate SPM across different particle composition categories. Therefore, accounting for particle composition can improve SPM estimates from optical observations, at least in some near-shore environments, such as those examined in this study. Additionally, the potential covariation between POC/SPM and the contributions of differently-sized particles to PSD reinforces the effectiveness of using POC/SPM as a proxy to classify coastal water types (Reynolds et al. 2016; Woźniak et al. 2010). Our particle composition-based classification approach improves SPM estimation across diverse coastal waters by capturing the variability of water types within these dynamic environments. Unlike other Optical Water Type (OWT) classification methods (Balasubramanian et al. 2020; Jiang et al. 2021) which are designed for a wide range of aquatic environments—rivers, lakes, estuaries, and coastal waters—our approach specifically accounts for varying particle composition across such diverse coastal environments. This approach allows for more accurate satellite-based mapping of SPM across diverse environments where sediment types and composition vary significantly. It is, however, also noteworthy that the importance of varying particle composition for estimating SPM may not be critical for all optically-complex marine environmental scenarios. For example, the study of a comprehensive field dataset from the Arctic environment by Stramski et al. (2023), which covered a very broad range of POC/SPM and SPM extending up to 20 g/m^3, indicated a robust capability to estimate SPM from optically-based algorithms without accounting for variations in POC/SPM.

For SPM estimation in different water types, we found that the prediction accuracy varies significantly across the spectrum of light wavelengths and exhibits unique trends for each water class (Fig. 8b). The red band provides better estimation for organic-rich particulate assemblages, while the NIR band is more effective for mineral-rich and extremely mineral-rich particulate assemblages. As the mineral fraction of SPM increases, the spectral peak of reflectance shifts gradually from blue to green, then to red, and finally to NIR (Fig. 8a). Therefore, while the red band reflectance is effective for predicting SPM in organic-rich water types, it becomes ineffective for mineral-rich water types, making the NIR band more suitable for these types. This explains why the single-band reflectance algorithms have difficulty estimating low SPM values, such as the algorithm of Doxaran et al. (2002) designed for highly turbid waters. Similarly, the algorithms by Miller and McKee (2004), Nechad et al. (2010), and Petus et al. (2010) face difficulties with both low and high SPM estimations due to the effect of reflectance saturation in the red band. Our proposed algorithms address this issue by switching the reflectance used in the algorithms to the appropriate spectral band for different water types, resulting in more accurate SPM estimation across a very wide range of SPM observed in diverse coastal waters.

4.2 Advancements and limitations of the new SPM retrieval algorithm

The presented SPM retrieval algorithm offers significant advancements in satellite-based mapping of sediment dynamics across various coastal environments. This algorithm improves the accuracy of SPM in different water types including organic-rich, mineral-rich, and extremely mineral-rich waters influenced by rivers, marshes, and marine environments. The algorithm is applicable to high spatial resolution land observation satellites (e.g., Landsat 5-9, Sentinel-2A/B, and

PlanetScope), enabling long-term, high spatial resolution mapping of SPM, and thus providing a tool for better understanding of sediment patterns and processes in coastal areas.

One of the key strengths of this algorithm is its applicability to most high spatial resolution land observation satellites, allowing it to capture fine-scale sediment patterns that cannot be detected by coarser-resolution ocean color satellites. For example, the SPM map obtained from Landsat imagery in Fig. 14a clearly shows sediment plumes along the coast and near river outlets along the northeast coast of the US. These detailed patterns reveal the sources of sediment and their transport trajectories, indicating that both coastal erosion and river discharge are crucial in supplying sediment to coastal environments such as marshes and beaches. Similarly, the SPM map in Fig. 14b captures fine-scale streaklines at the outlet of the Atchafalaya River. These filament-like, flow-parallel patterns provide insights into subsurface bathymetry and flow direction (Ayoub et al. 2018), demonstrating the algorithm ability to detect subtle changes in sediment dynamics that coarser sensors might miss.

The proposed algorithm also captures seasonal variability in SPM. For instance, in San Francisco Bay (Fig. 15a), SPM shows significant seasonal fluctuations with higher SPM levels during spring and summer and lower values in autumn and winter. These changes are likely driven by seasonal variations in wind speed, which enhance sediment resuspension and transport (Schoellhamer et al. 2007). In the northeastern US (Fig. 15b), SPM levels rise during winter and spring due to storms and increased offshore wave activity, which are key drivers of sediment dynamics in this region (Baranes et al. 2022; Yellen et al. 2023). In contrast, SPM in the Atchafalaya River Delta peaks in May and is lower in autumn (Fig. 15c), reflecting the seasonal patterns of river discharge which is the primary source of sediment for the delta (Rosen and Xu 2013). These examples highlight the algorithm capability to adequately capture seasonal changes in SPM across different coastal environments.

In addition to seasonal variability, the algorithm provides valuable insights into long-term SPM dynamics. Fig. 16a illustrates a contrasting increase in SPM in Lake Pontchartrain and a decrease in the Atchafalaya River and its delta. The increase in SPM in Lake Pontchartrain is likely due to more frequent use of the Bonne Carre Spillway, which diverts Mississippi River water into the lake during high flows. The use of Spillway has increased dramatically in recent years, introducing more sediment from the Mississippi River into the lake (Allison et al. 2013). On the other hand, the decrease in SPM in the Atchafalaya River and delta can be attributed to the impact of damming and river management (Meade and Moody 2009). Similarly, Fig. 16b shows an increase in SPM in the upper region of Blackwater and a decrease in Fishing Bay. The increased SPM in the Blackwater National Wildlife Refuge is possibly due to the degradation of tidal marshes which release sediment into the water column (Ganju et al. 2015; Hopkinson et al. 2018), while the reduced levels of SPM in Fishing Bay are likely due to a decreased sediment supply from various sources (Turner et al. 2021). These results demonstrate the algorithm effectiveness in capturing long-term trends in SPM, allowing for a better understanding of how natural and anthropogenic factors influence sediment dynamics over time.

Overall, the new SPM retrieval algorithm significantly improves our ability to monitor and understand coastal sediment dynamics both at fine spatial scales and over extended temporal periods. Its adaptability to different water types and high spatial resolution capabilities of satellites makes it an effective tool for studying coastal environments and understanding the processes that influence them.

Even though the new algorithm has been validated using both SPM and water turbidity measurements across several sites, demonstrating its capability to detect spatial and temporal changes, it still has limitations. The empirical approach presented in this paper was calibrated using field data compiled from a limited number of sites. Consequently, it may not perform well for water types that are not well represented in the calibration dataset. More field data are necessary for further evaluation of the algorithm, especially for site-specific research. The algorithm parameters may need to be adjusted based on local conditions. Beyond the algorithm itself, the satellite mapping of SPM product developed in this study also has some limitations and should be used with caution. Various factors, including atmospheric correction, bottom reflectance, adjacency effects, will contribute to the uncertainty of satellite-derived SPM. In this study, we used an empirical line method based on 14 matchups to correct Landsat Surface Reflectance (SR) images to removing the contributions of light reflected at the air-water interface and better align the SR values with field-measured spectral remote-sensing reflectance, $R_{rs}(\lambda)$. The results show good agreement with field-measured $R_{rs}(\lambda)$ and are supported by findings from Page et al. (2019). Their study demonstrated that atmospherically corrected Landsat SR shapes and magnitudes are comparable to those produced by other ocean color-specific atmospheric correction methods (e.g., ACOLITE and MAIN). However, the simple empirical atmospheric correction method used in this study may involve significant uncertainties when applied globally to coastal waters. For global SPM studies, more robust atmospheric correction algorithms are still needed. Furthermore, this study did not account for the effects of bottom reflectance or land adjacency effects on satellite-based estimation of SPM. As a result, the algorithm may be less reliable in optically shallow waters or areas very close to the coast where these effects are significant. Addressing these factors will be essential for improving SPM estimation in such regions.

4.3 Landsat temporal coverage for capturing coastal sediment dynamics

High-intensity and lower-frequency tidal and wave activities, as well as storm events, play a significant role in remobilizing coastal suspended sediment (Cortese et al. 2024; Traykovski et al. 2004). While it is not feasible for Landsat to consistently capture short-lived events and extreme values (the revisit time of a single Landsat mission is 16 days), we postulate that Landsat can capture the distribution and variability patterns of SPM at a given coastal location with a sufficient number of repeated satellite observations. To test this, we compared histograms of the continuous turbidity measurements with a subset of turbidity data during satellite overpasses over one-year and five-year periods for the Atchafalaya River (LA) (station ID: 07381600) (Fig. 17).

The one-year satellite observations (Fig. 17a) suggest a larger discrepancy between in situ turbidity measurements and in situ turbidity measurements that correspond to satellite overpass, particularly in the higher percentiles (top 2%, top 5%, and top 10%). However, none of these differences were statistically significant at the 0.05 level. For instance, the independent t-test comparing the means yielded a p-value of 0.0855, indicating the means are not significantly different. The Mann-Whitney U test for examining the medians yielded $p = 0.2138$, indicating no significant difference in this central tendency. The Kolmogorov-Smirnov test which compares the overall distribution showed $p = 0.1349$, suggesting more divergence in the distributions although still not statistically significant. For the one-year observations, wider confidence intervals (CIs) were found in the top percentiles. For example, the 98th percentile CI was [0.0, 71.51] which indicates substantial uncertainty in the estimate of the difference. The wide CIs reflect that the difference between in situ turbidity measurements and in situ turbidity measurements coincident with satellite overpass could vary more widely. Although the differences were not statistically significant, the higher percentiles suggest that turbidity measured at satellite overpass consistently reported lower turbidity than the continuously measured turbidity due to missing extreme events.

In contrast, the five-year satellite observations (Fig. 17b) captured a more representative range of turbidity conditions including higher turbidity events. The independent t-test on the five-year data showed the *p*-value of 0.9897, suggesting no significant difference in the means between the two datasets. The Mann-Whitney U test for medians ($p = 0.8021$) and the Kolmogorov-Smirnov test ($p = 0.3636$) further confirm that there was no significant difference between the distributions of turbidity in this period. The narrower CIs in the five-year dataset (e.g., 98th percentile CI = [-17.0, 26.0]) indicate less variability and higher confidence in the ability of the satellite observation to capture representative turbidity events. This result suggests that a longer time frame, such as five years, is essential for capturing episodic events and the full variability of sediment dynamics in coastal areas. The consistency between the two groups over five years demonstrates that extended datasets significantly reduce the differences observed over shorter time frames.

In conclusion, while one-year data may provide insights into general trends, the observed difference in the higher percentiles and the wider confidence intervals highlight the limitations of short-term observations. For a robust analysis of sediment dynamics, particularly during episodic high-turbidity events, at least five years of Landsat data are required to obtain a representative and statistically comparable observation. However, to study short-term events such as storms, the application of this algorithm to high spatial and temporal resolution satellites (e.g., Sentinel-2, PlanetScope) will provide a significant advantage by enhancing the temporal frequency of SPM observations in coastal regions.

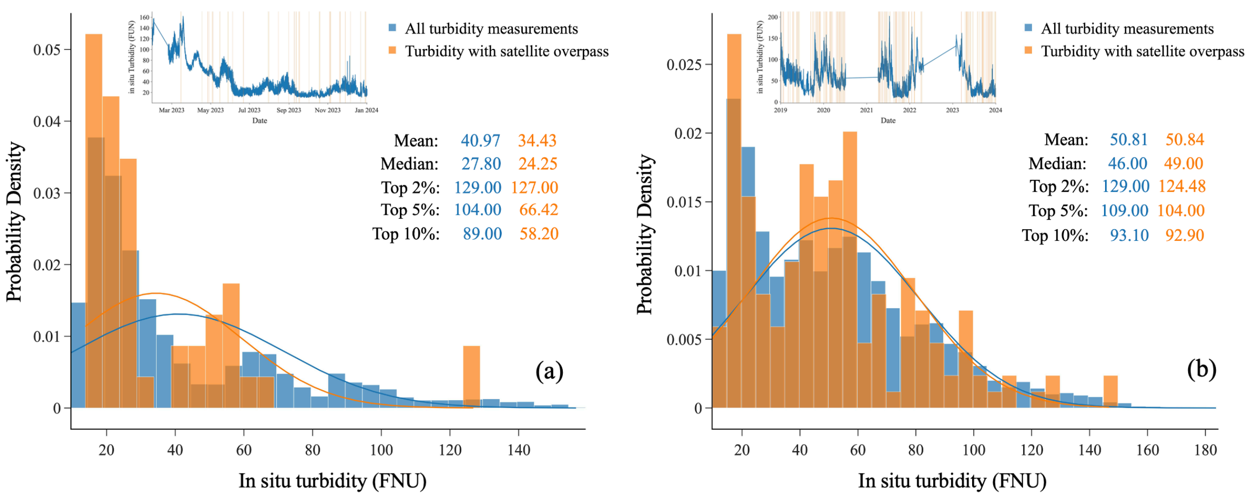

Figure 17. Histograms of all turbidity measurements compared to those taken during Landsat satellite overpasses over one-year (a) and five-year (b) periods for the Atchafalaya River (LA). The inset plot shows continuous turbidity measurements alongside turbidity data obtained during satellite overpasses.

5. Summary and Conclusions

In this paper, we present a new SPM retrieval algorithm for application of satellite remote sensing with land observation sensors in optically-complex coastal waters with varied sources of suspended particles. The major contributions of this work include: (i) we compiled a dataset of in situ spectral reflectance and SPM measurements covering a wide range of particulate concentrations and chemical compositions from river-, marsh-, and marine-influenced coastal waters; (ii) we developed an algorithm for remote sensing applications which includes the classification of water types into organic-rich, mineral-rich, and extremely mineral-rich particle composition types using POC/SPM derived from remote-sensing reflectance $R_{rs}(\lambda)$ and a subsequent use of particle composition-specific algorithms to estimate SPM from $R_{rs}(\lambda)$ in different water types; (iii) we compared the performance of the proposed SPM retrieval algorithm with eight previously published SPM algorithms including empirical, semi-analytical, and machine learning models, which showed reliable and generally improved SPM estimations from our algorithm; (iv) we developed an empirical method to correct Landsat radiometry in the GEE environment to improve the satellite estimation of remote-sensing reflectance and applied our particle composition-specific SPM retrieval algorithm to Landsat images from the past four decades (1984–2023); (v) we validated our SPM satellite mapping results using satellite-in situ matchup dataset and in situ water turbidity measurements across different coastal environments, and (vi) we demonstrated the ability of the proposed remote sensing algorithms to study long-term coastal SPM at high spatial resolution from land observation satellites, in particular the Landsat satellite mission. The high resolution of the SPM mapping can capture fine-scale SPM patterns along the coast and also capture seasonal and long-term variability in different coastal environments. Our results collectively demonstrate the promise of this new SPM retrieval algorithm for studying the coastal suspended sediment dynamics from satellite observations at local, regional, and global scales.

Acknowledgements

The research was supported by U.S. Geological Survey and a Department of Interior Northeast Climate Adaptation Science Center (NECASC): No. G20AC00071.

References

Allen, J. R. (2000). Morphodynamics of Holocene salt marshes: a review sketch from the Atlantic and Southern North Sea coasts of Europe. Quaternary Science Reviews, 19(12), 1155-1231. https://doi.org/10.1016/S0277-3791(99)00034-7.

Allison, M. A., Vosburg, B. M., Ramirez, M. T., & Meselhe, E. A. (2013). Mississippi River channel response to the Bonnet Carré Spillway opening in the 2011 flood and its implications for the design and operation of river diversions. Journal of Hydrology, 477, 104-118. https://doi.org/10.1016/j.jhydrol.2012.11.011.

Androulidakis, Y. S., & Kourafalou, V. H. (2013). On the processes that influence the transport and fate of Mississippi waters under flooding outflow conditions. Ocean Dynamics, 63, 143-164. https://doi.org/10.1007/s10236-012-0587-8.

Ayoub, F., Jones, C. E., Lamb, M. P., Holt, B., Shaw, J. B., Mohrig, D., & Wagner, W. (2018). Inferring surface currents within submerged, vegetated deltaic islands and wetlands from multi-pass airborne SAR. Remote Sensing of Environment, 212, 148-160. https://doi.org/10.1016/j.rse.2018.04.035.

Balasubramanian, S.V., Pahlevan, N., Smith, B., Binding, C., Schalles, J., Loisel, H., Gurlin, D., Greb, S., Alikas, K., Randla, M., Bunkei, M., Moses, W., N, H., Lehmann, M.K., O'Donnell, D., Ondrusek, M., Han, T.H., Fichot, C.G., Moore, T., & Boss, E. (2020). Robust algorithm for estimating total suspended solids (TSS) in inland and nearshore coastal waters. Remote Sensing of Environment, 246, 111768. https://doi.org/10.1016/j.rse.2020.111768.

Baranes, H. E., Woodruff, J. D., Geyer, W. R., Yellen, B. C., Richardson, J. B., & Griswold, F. (2022). Sources, mechanisms, and timescales of sediment delivery to a New England salt marsh. Journal of Geophysical Research: Earth Surface, 127(3), e2021JF006478. https://doi.org/10.1029/2021JF006478.

Barbier, E. B., Hacker, S. D., Kennedy, C., Koch, E. W., Stier, A. C., & Silliman, B. R. (2011). The value of estuarine and coastal ecosystem services. Ecological Monographs, 81(2), 169-193. https://doi.org/10.1890/10-1510.1.

Bhargava, D. S., & Mariam, D. W. (1991). Effects of suspended particle size and concentration on reflectance measurements. Photogrammetric Engineering and Remote Sensing, 57(5), 519-529.

Bi, S., & Hieronymi, M. (2024). Holistic optical water type classification for ocean, coastal, and inland waters. Limnology and Oceanography, 69(7), 1547-1561. https://doi.org/10.1002/lno.12606.

Bianchi, T. S. (2011). The role of terrestrially derived organic carbon in the coastal ocean: A changing paradigm and the priming effect. Proceedings of the National Academy of Sciences, 108(49), 19473-19481. https://doi.org/10.1073/pnas.101798210.

Boss, E., Pegau, W.S., Gardner, W.D., Zaneveld, J.R.V., Barnard, A.H., Twardowski, M.S., Chang, G.C., & Dickey, T.D. (2001). Spectral particulate attenuation and particle size distribution in the bottom boundary layer of a continental shelf. Journal of Geophysical Research: Oceans, 106(C5), 9509-9516. https://doi.org/10.1029/2000JC900077.

Boss, E., Pegau, W. S., Lee, M., Twardowski, M., Shybanov, E., Korotaev, G., & Baratange, F. (2004). Particulate backscattering ratio at LEO 15 and its use to study particle composition and distribution. Journal of Geophysical Research: Oceans, 109, C01014. https://doi.org/10.1029/2002JC001514.

Cahoon, D. R., Lynch, J. C., Roman, C. T., Schmit, J. P., & Skidds, D. E. (2019). Evaluating the relationship among wetland vertical development, elevation capital, sea-level rise, and tidal marsh sustainability. Estuaries and Coasts, 42, 1-15. https://doi.org/10.1007/s12237-018-0448-x.

Castagna, A., Amadei Martínez, L., Bogorad, M., Daveloose, I., Dasseville, R., Dierssen, H.M., Beck, M., Mortelmans, J., Lavigne, H., Dogliotti, A., Doxaran, D., Ruddick, K., Vyverman, W., & Sabbe, K. (2022). Optical and biogeochemical properties of diverse Belgian inland and coastal waters. Earth System Science Data, 14(6), 2697-2719. https://doi.org/10.5194/essd-14-2697-2022.

Coleman, D. J., Schuerch, M., Temmerman, S., Guntenspergen, G., Smith, C. G., & Kirwan, M. L. (2022). Reconciling models and measurements of marsh vulnerability to sea level rise. Limnology and Oceanography Letters, 7(2), 140-149. https://doi.org/10.1002/lol2.10230.

Cortese, L., Zhang, X., Simard, M., & Fagherazzi, S. (2024). Storm impacts on mineral mass accumulation rates of coastal marshes. Journal of Geophysical Research: Earth Surface, 129(3), e2023JF007065. https://doi.org/10.1029/2023JF007065.

Dethier, E., Renshaw, C., & Magilligan, F. (2020). Toward improved accuracy of remote sensing approaches for quantifying suspended sediment: Implications for suspended-sediment monitoring. Journal of Geophysical Research: Earth Surface, 125(7), e2019JF005033. https://doi.org/10.1029/2019JF005033.

Doxaran, D., Froidefond, J. M., Lavender, S., & Castaing, P. (2002). Spectral signature of highly turbid waters: Application with SPOT data to quantify suspended particulate matter concentrations. Remote Sensing of Environment, 81(1), 149-161. https://doi.org/10.1016/S0034-4257(01)00341-8.

Ensign, S. H., Halls, J. N., & Peck, E. K. (2023). Watershed sediment cannot offset sea level rise in most US tidal wetlands. Science, 382(6675), 1191-1195. 10.1126/science.adj0513.

Fagherazzi, S., Mariotti, G., Leonardi, N., Canestrelli, A., Nardin, W., & Kearney, W. S. (2020). Salt marsh dynamics in a period of accelerated sea level rise. Journal of Geophysical Research: Earth Surface, 125(8), e2019JF005200. https://doi.org/10.1029/2019JF005200.

Fagherazzi, S., Mariotti, G., Wiberg, P. L., & McGLATHERY, K. J. (2013). Marsh collapse does not require sea level rise. Oceanography, 26(3), 70-77. https://doi.org/10.5670/oceanog.2013.47.

Fichot, C.G., and J. Harringmeyer. (2023). Delta-X: In Situ Water Surface Reflectance across MRD, LA, USA, 2021, V3. ORNL DAAC, Oak Ridge, Tennessee, USA. https://doi.org/10.3334/ORNLDAAC/2153.

Ganju, N. K., Defne, Z., Kirwan, M. L., Fagherazzi, S., D'Alpaos, A., & Carniello, L. (2017). Spatially integrative metrics reveal hidden vulnerability of microtidal salt marshes. Nature communications, 8(1), 14156. https://doi.org/10.1038/ncomms14156.

Ganju, N. K., Kirwan, M. L., Dickhudt, P. J., Guntenspergen, G. R., Cahoon, D. R., & Kroeger, K. D. (2015). Sediment transport-based metrics of wetland stability. Geophysical Research Letters, 42(19), 7992-8000. https://doi.org/10.1002/2015GL065980.

Gordon, H. (2019). Physical Principles of Ocean Color Remote Sensing. https://doi.org/10.33596/ppocrs-19.

Han, B., Loisel, H., Vantrepotte, V., Meriaux, X., Bryere, P., Ouillon, S., Dessailly, D., Xing, Q., Zhu, J., 2016. Development of a semi-analytical algorithm for the retrieval of suspended particulate matter from remote sensing over clear to very turbid waters. Remote Sens. 8, 211. https://doi.org/10.3390/rs8030211.

Hopkinson, C. S., Morris, J. T., Fagherazzi, S., Wollheim, W. M., & Raymond, P. A. (2018). Lateral marsh edge erosion as a source of sediments for vertical marsh accretion. Journal of Geophysical Research: Biogeosciences, 123(8), 2444-2465. https://doi.org/10.1029/2017JG004358.

Hopkinson, C. S., Wolanski, E., Cahoon, D. R., Perillo, G. M., & Brinson, M. M. (2019). Coastal wetlands: a synthesis. In Coastal wetlands (pp. 1-75). Elsevier. https://doi.org/10.1016/B978-0-444-63893-9.00001-0.

Jerlov, N.G., 1976. Marine Optics. Elsevier, Amsterdam.

Jiang, D., Matsushita, B., Pahlevan, N., Gurlin, D., Lehmann, M.K., Fichot, C.G., Schalles, J., Loisel, H., Binding, C., Zhang, Y.L., Alikas, K., Kangro, K., Uusoue, M., Ondrusek, M., Greb, S., Moses, W.J., Lohrenz, S., & O 'Donnell, D. (2021). Remotely estimating total suspended solids concentration in clear to extremely turbid waters using a novel semi-analytical method. Remote Sensing of Environment, 258, 112386. https://doi.org/10.1016/j.rse.2021.112386.

Jonasz, M., Fournier, G.R., 2007. Light Scattering by Particles in Water. Theoretical and Experimental Foundations. Academic Press, Amsterdam.

Kirk, J. T. (1994). Light and photosynthesis in aquatic ecosystems. Cambridge university press.

Kirwan, M. L., & Guntenspergen, G. R. (2012). Feedbacks between inundation, root production, and shoot growth in a rapidly submerging brackish marsh. Journal of Ecology, 100(3), 764-770. https://doi.org/10.1111/j.1365-2745.2012.01957.x.

Kirwan, M. L., & Megonigal, J. P. (2013). Tidal wetland stability in the face of human impacts and sea-level rise. Nature, 504(7478), 53-60. https://doi.org/10.1038/nature12856.

Ladd, C. J., Duggan-Edwards, M. F., Bouma, T. J., Pagès, J. F., & Skov, M. W. (2019). Sediment supply explains long-term and large-scale patterns in salt marsh lateral expansion and erosion. Geophysical Research Letters, 46(20), 11178-11187. https://doi.org/10.1029/2019GL083315.

Lehmann, M.K., Gurlin, D., Pahlevan, N., Alikas, K., Conroy, T., Anstee, J., Balasubramanian, S.V., Barbosa, C.C.F., Binding, C., Bracher, A., Bresciani, M., Burtner, A., Cao, Z., Dekker, A.G., Di Vittorio, C., Drayson, N., Errera, R.M., Fernandez, V., Ficek, D., Fichot, C.G., Gege, P., Giardino, C., Gitelson, A.A., Greb, S.R., Henderson, H., Higa, H., Rahaghi, A.I., Jamet, C., Jiang, D., Jordan, T., Kangro, K., Kravitz, J.A., Kristoffersen, A.S., Kudela, R., Li, L., Ligi, M., Loisel, H., Lohrenz, S., Ma, R., Maciel, D.A., Malthus, T.J., Matsushita, B., Matthews, M., Minaudo, C., Mishra, D.R., Mishra, S., Moore, T., Moses, W.J., Nguyễn, H., Novo, E.M.L.M., Novoa, S., Odermatt, D., O'Donnell, D.M., Olmanson, L.G., Ondrusek, M., Oppelt, N., Ouillon, S., Pereira Filho, W., Plattner, S., Verdú, A.R., Salem, S.I., Schalles, J.F., Simis, S.G.H., Siswanto, E., Smith, B., Somlai-Schweiger, I., Soppa, M.A., Spyrakos, E., Tessin, E., van der Woerd, H.J., Vander Woude, A., Vandermeulen, R.A., Vantrepotte, V., Wernand, M.R., Werther, M., Young, K., & Yue, L. (2023). GLORIA-A globally representative hyperspectral in situ dataset for optical sensing of water quality. Scientific data, 10(1), 100. https://doi.org/10.1038/s41597-023-01973-y.

McFeeters, S. K. (1996). The use of the Normalized Difference Water Index (NDWI) in the delineation of open water features. International journal of remote sensing, 17(7), 1425-1432. https://doi.org/10.1080/01431169608948714.

McKeon, K., Woodruff, J. D., Yellen, B., Fernald, S. H., & Sheehan, M. C. (2022). Invasive water chestnut hinders tidal wetland development. Earth Surface Processes and Landforms, 47(6), 1409-1424. https://doi.org/10.1002/esp.5323.

Meade, R. H., & Moody, J. A. (2010). Causes for the decline of suspended-sediment discharge in the Mississippi River system, 1940–2007. Hydrological Processes: An International Journal, 24(1), 35-49. https://doi.org/10.1002/hyp.7477.

Mélin, F., & Vantrepotte, V. (2015). How optically diverse is the coastal ocean?. Remote Sensing of Environment, 160, 235-251. https://doi.org/10.1016/j.rse.2015.01.023.

Miller, R. L., & McKee, B. A. (2004). Using MODIS Terra 250 m imagery to map concentrations of total suspended matter in coastal waters. Remote Sensing of Environment, 93(1-2), 259-266. https://doi.org/10.1016/j.rse.2004.07.012.

Milliman, J. D. (1997). Fluvial sediment discharge to the sea and the importance of regional tectonics. In Tectonic uplift and climate change (pp. 239-257). Boston, MA: Springer US. https://doi.org/10.1007/978-1-4615-5935-1_10.

Milliman, J. D., & Syvitski, J. P. (1992). Geomorphic/tectonic control of sediment discharge to the ocean: the importance of small mountainous rivers. The journal of Geology, 100(5), 525-544. https://doi.org/10.1086/629606.

Minella, J. P., Merten, G. H., Reichert, J. M., & Clarke, R. T. (2008). Estimating suspended sediment concentrations from turbidity measurements and the calibration problem. Hydrological Processes: An International Journal, 22(12), 1819-1830. https://doi.org/10.1002/hyp.6763.

Mobley, C. (2022). The Oceanic Optics Book.

Moore, T. S., Campbell, J. W., & Feng, H. (2001). A fuzzy logic classification scheme for selecting and blending satellite ocean color algorithms. IEEE Transactions on Geoscience and Remote sensing, 39(8), 1764-1776. 10.1109/36.942555.

Mudd, S. M., Fagherazzi, S., Morris, J. T., & Furbish, D. J. (2004). Flow, sedimentation, and biomass production on a vegetated salt marsh in South Carolina: toward a predictive model of marsh morphologic and ecologic evolution. The ecogeomorphology of tidal marshes, 59, 165-188. https://doi.org/10.1029/CE059p0165.

Nechad, B., Ruddick, K. G., & Park, Y. (2010). Calibration and validation of a generic multisensor algorithm for mapping of total suspended matter in turbid waters. Remote Sensing of Environment, 114(4), 854-866. https://doi.org/10.1016/j.rse.2009.11.022.

Novoa, S., Doxaran, D., Ody, A., Vanhellemont, Q., Lafon, V., Lubac, B., & Gernez, P. (2017). Atmospheric corrections and multi-conditional algorithm for multi-sensor remote sensing of suspended particulate matter in low-to-high turbidity levels coastal waters. Remote Sensing, 9(1), 61. https://doi.org/10.3390/rs9010061.

O'Connell, J. F. (2010). Shoreline armoring impacts and management along the shores of Massachusetts and Kauai, Hawaii. In Puget Sound Shorelines and the Impacts of Armoring--Proceedings of State of the Science Workshop (pp. 65-76).

Page, B. P., Olmanson, L. G., & Mishra, D. R. (2019). A harmonized image processing workflow using Sentinel-2/MSI and Landsat-8/OLI for mapping water clarity in optically variable lake systems. Remote Sensing of Environment, 231, 111284. https://doi.org/10.1016/j.rse.2019.111284.

Pekel, J. F., Cottam, A., Gorelick, N., & Belward, A. S. (2016). High-resolution mapping of global surface water and its long-term changes. Nature, 540(7633), 418-422. https://doi.org/10.1038/nature20584.

Peteet, D.M., Nichols, J., Kenna, T., Chang, C., Browne, J., Reza, M., Kovari, S., Liberman, L., & Stern-Protz, S. (2018). Sediment starvation destroys New York City marshes' resistance to sea level rise. Proceedings of the National Academy of Sciences, 115(41), 10281-10286. https://doi.org/10.1073/pnas.1715392115.

Petus, C., Chust, G., Gohin, F., Doxaran, D., Froidefond, J. M., & Sagarminaga, Y. (2010). Estimating turbidity and total suspended matter in the Adour River plume (South Bay of Biscay) using MODIS 250-m imagery. Continental Shelf Research, 30(5), 379-392. https://doi.org/10.1016/j.csr.2009.12.007.

Reynolds, R. A., Stramski, D., & Neukermans, G. (2016). Optical backscattering by particles in Arctic seawater and relationships to particle mass concentration, size distribution, and bulk composition. Limnology and Oceanography, 61(5), 1869-1890. https://doi.org/10.1002/lno.10341.

Rosen, T., & Xu, Y. J. (2013). Recent decadal growth of the Atchafalaya River Delta complex: Effects of variable riverine sediment input and vegetation succession. Geomorphology, 194, 108-120. https://doi.org/10.1016/j.geomorph.2013.04.020.

Salter, G., Passalacqua, P., Wright, K., Feil, S., Jensen, D., Simard, M., & Lamb, M. P. (2022). Spatial patterns of deltaic deposition/erosion revealed by streaklines extracted from remotely-sensed suspended sediment concentration. Geophysical Research Letters, 49(11), e2022GL098443. https://doi.org/10.1029/2022GL098443.

Schoellhamer, D. H., Mumley, T. E., & Leatherbarrow, J. E. (2007). Suspended sediment and sediment-associated contaminants in San Francisco Bay. Environmental Research, 105(1), 119-131. https://doi.org/10.1016/j.envres.2007.02.002.

Sen, P. K. (1968). Estimates of the regression coefficient based on Kendall's tau. Journal of the American statistical association, 63(324), 1379-1389. https://doi.org/10.1080/01621459.1968.10480934.

Skakun, S., Vermote, E. F., Roger, J. C., Justice, C. O., & Masek, J. G. (2019). Validation of the LaSRC cloud detection algorithm for Landsat 8 images. IEEE Journal of Selected Topics in Applied Earth Observations and Remote Sensing, 12(7), 2439-2446. 10.1109/JSTARS.2019.2894553.

Stramski, D., Boss, E., Bogucki, D., & Voss, K. J. (2004). The role of seawater constituents in light backscattering in the ocean. Progress in Oceanography, 61(1), 27-56. https://doi.org/10.1016/j.pocean.2004.07.001.

Stramski, D., Constantin, S., & Reynolds, R. A. (2023). Adaptive optical algorithms with differentiation of water bodies based on varying composition of suspended particulate matter: A case study for estimating the particulate organic carbon concentration in the western Arctic seas. Remote Sensing of Environment, 286, 113360. https://doi.org/10.1016/j.rse.2022.113360.

Sweet, J.A., Bargu, S., Morrison, W.L., Parsons, M., Pathare, M.G., Roberts, B.J., Soniat, T.M., & Stauffer, B.A. (2022). Phytoplankton dynamics in Louisiana estuaries: building a baseline to understand current and future change. Marine Pollution Bulletin, 175, 113344. https://doi.org/10.1016/j.marpolbul.2022.113344.

Syvitski, J. P., & Kettner, A. (2011). Sediment flux and the Anthropocene. Philosophical Transactions of the Royal Society A: Mathematical, Physical and Engineering Sciences, 369(1938), 957-975. https://doi.org/10.1098/rsta.2010.0329.

Traykovski, P., Geyer, R., & Sommerfield, C. (2004). Rapid sediment deposition and fine-scale strata formation in the Hudson estuary. Journal of Geophysical Research: Earth Surface, 109, F02004. https://doi.org/10.1029/2003JF000096.

Turner, J. S., St-Laurent, P., Friedrichs, M. A., & Friedrichs, C. T. (2021). Effects of reduced shoreline erosion on Chesapeake Bay water clarity. Science of the Total Environment, 769, 145157. https://doi.org/10.1016/j.scitotenv.2021.145157.

Twardowski, M. S., Boss, E., Macdonald, J. B., Pegau, W. S., Barnard, A. H., & Zaneveld, J. R. V. (2001). A model for estimating bulk refractive index from the optical backscattering ratio and the implications for understanding particle composition in case I and case II waters. Journal of Geophysical Research: Oceans, 106(C7), 14129-14142. https://doi.org/10.1029/2000JC000404.

Vanhellemont, Q. (2019). Adaptation of the dark spectrum fitting atmospheric correction for aquatic applications of the Landsat and Sentinel-2 archives. Remote Sensing of Environment, 225, 175-192. https://doi.org/10.1016/j.rse.2019.03.010

Volpe, V., Silvestri, S., & Marani, M. (2011). Remote sensing retrieval of suspended sediment concentration in shallow waters. Remote sensing of Environment, 115(1), 44-54. https://doi.org/10.1016/j.rse.2010.07.013.

Walker, N. D. (2001). Tropical storm and hurricane wind effects on water level, salinity, and sediment transport in the river-influenced Atchafalaya-Vermilion Bay system, Louisiana, USA. Estuaries, 24, 498-508. https://doi.org/10.2307/1353252.

Walling, D. E. (2008). The changing sediment loads of the world's rivers. Annals of Warsaw University of Life Sciences-SGGW. Land Reclamation, (39). 10.2478/v10060-008-0001-x.

Weston, N. B. (2014). Declining sediments and rising seas: an unfortunate convergence for tidal wetlands. Estuaries and Coasts, 37(1), 1-23. https://doi.org/10.1007/s12237-013-9654-8.

Windham-Myers, L., Crooks, S., & Troxler, T. G. (Eds.). (2018). A blue carbon primer: the state of coastal wetland carbon science, practice and policy. CRC Press.

Wolfe, R., Masek, J., Saleous, N., & Hall, F. (2004, September). LEDAPS: mapping North American disturbance from the Landsat record. In IGARSS 2004. 2004 IEEE International Geoscience and Remote Sensing Symposium (Vol. 1). IEEE.

Woźniak, S.B., Stramski, D., Stramska, M., Reynolds, R.A., Wright, V.M., Miksic, E.Y., Cichocka, M., & Cieplak, A.M. (2010). Optical variability of seawater in relation to particle concentration, composition, and size distribution in the nearshore marine environment at Imperial Beach, California. Journal of Geophysical Research: Oceans, 115, C08027. https://doi.org/10.1029/2009JC005554.

Xue, K., Zhang, Y., Duan, H., Ma, R., Loiselle, S., & Zhang, M. (2015). A remote sensing approach to estimate vertical profile classes of phytoplankton in a eutrophic lake. Remote Sensing, 7(11), 14403-14427. https://doi.org/10.3390/rs71114403.

Yellen, B., Woodruff, J. D., Baranes, H. E., Engelhart, S. E., Geyer, W. R., Randall, N., & Griswold, F. R. (2023). Salt marsh response to inlet switch-induced increases in tidal inundation. Journal of Geophysical Research: Earth Surface, 128(1), e2022JF006815. https://doi.org/10.1029/2022JF006815.

Yu, X., Lee, Z., Shen, F., Wang, M., Wei, J., Jiang, L., & Shang, Z. (2019). An empirical algorithm to seamlessly retrieve the concentration of suspended particulate matter from water color across ocean to turbid river mouths. Remote Sensing of Environment, 235, 111491. https://doi.org/10.1016/j.rse.2019.111491.

Zhang, X.H., Fichot, C.G., Baracco, C., Guo, R.Z., Neugebauer, S., Bengtsson, Z., Ganju, N., & Fagherazzi, S. (2020). Determining the drivers of suspended sediment dynamics in tidal marsh-influenced estuaries using high-resolution ocean color remote sensing. Remote Sensing of Environment, 240, 111682. https://doi.org/10.1016/j.rse.2020.111682.

List of Figure Captions:

Figure 1. The interaction of light with suspended sediments, phytoplankton, organic detritus, colored dissolved organic matter, and water molecules plays a crucial role in determining remotely sensed ocean color. This diagram illustrates how light interacts with suspended particles originating from various sources, including riverine sediment (1), marsh edge erosion and local resuspension (2), marine sediment from coastal erosion (3), and phytoplankton.

Figure 2. Comparison between an ocean color sensor (MODIS) and a land observation sensor (Landsat). (a) MODIS-Terra Surface Reflectance on Google Earth Engine (GEE) (b) Landsat 8 Surface Reflectance on GEE. Both images are displayed in true color.

Figure 3. The geographical distributions of the compiled in situ datasets. Each panel shows the locations of in situ measurements in yellow dots for different study sites. The number of samples (*n*) is indicated for each site, along with the sediment source type (river-influenced, marsh-influenced, or marine-influenced). (a) Atchafalaya River, (b) Terrebonne Basin, (c) Arctic Ocean, (d) Red River, (e) Mekong River, (f) Gironde River, (g) Gulf of Mexico, (h) Yellow Sea, (i) Seto-Inland Sea, (j) Hawke Bay, (k) English Channel, and (l) Plum Island.

Figure 4. Probability distribution of SPM (a), POC (b) and POC/SPM (c) in marine-influenced, marsh-influenced, and river-influenced waters.

Figure 5. In situ spectral curve for constant SPM and varied POC/SPM ratio as labeled. (a) SPM = 6 g/m^3. (b) SPM = 10 g/m^3. (c) SPM = 20 g/m^3. (d) SPM = 40 g/m^3.

Figure 6. Algorithm-derived versus measured values of POC/SPM using different algorithms applied to the in situ dataset. (a) Blue band algorithm. (b) Green band algorithm. (c) Red band algorithm. (d) Three-bands algorithm.

Figure 7. Example spectra of $R_{rs}(\lambda)$ from in situ observations for different particle composition classes where each spectral curve represents a single hyperspectral measurement. (a) Organic-rich particle class from Mekong River. (b) Organic-rich particle class from Terrebonne. (c) Mineral-rich particle class from English Channel and Hawke Bay. (d) Mineral-rich particle class from Terrebonne. (e) Extremely mineral-rich (E) particle class from Gironde River. (f) Extremely mineral-rich (E) particle class from English Channel. The vertical dashed lines correspond to wavelengths of 490 nm, 555 nm, 670 nm, and 810 nm.

Figure 8. (a) Example $R_{rs}(\lambda)$ spectra for the three water types from in situ measurements. The shaded regions represent the interquartile range (IQR, 25th–75th percentile), while the solid line with circular markers indicates the median R_{rs} at each wavelength. Wavelengths are shown at 10 nm intervals from 400 nm to 890 nm for illustrative purposes. (b) The R^2 values of linear regression between log-transformed SPM and $R_{rs}(\lambda)$ from 400 to 890 nm for three particle composition classes.

Figure 9. Measured SPM versus in situ R_{rs} (Red = 670 nm and NIR = 810 nm) for the three particle composition classes. (a) SPM vs. $R_{rs}(670)$ for organic-rich particle class. (b) SPM vs. $R_{rs}(670)$ for mineral-rich class. (c) SPM vs. $R_{rs}(670)$ for extremely mineral-rich class. (d) SPM vs. $R_{rs}(810)$ for organic-rich class. (e) SPM vs. $R_{rs}(810)$ for mineral-rich class. (f) SPM vs. $R_{rs}(810)$ for extremely mineral-rich class.

Figure 10. Algorithm-derived versus measured values of SPM using our particle composition-specific SPM retrieval algorithm with data points color coded according to the predicted POC/SPM values obtained from our green band POC/SPM algorithm. The SPM values were estimated from in situ R_{rs} measurements at a single band for different sites according to the water type classification in terms of particle composition parameter POC/SPM. (a) Gulf of Mexico, (b) Yellow Sea, (c) Arctic Ocean, (d) Hawke Bay, (e) Seto-Inland Sea, (f) English Channel, (g) Terrebonne, (h) Plum Island, (i) Mekong River, (j) Atchafalaya, (k) Red River, and (l) Gironde River. The sample size is slightly different from that in Table 1 because the mineral-rich samples at some sites lack in situ measurement of $R_{rs}(810)$.

Figure 11. Comparison of algorithm-derived SPM with in situ measurements of SPM. The estimated SPM values were obtained from in situ-measured $R_{\mathrm{rs}}(\lambda)$ using different SPM algorithms. (a) Doxaran (2002). (b) Miller and McKee (2004). (c) Nechad (2010). (d) Petus (2010). (e) Novoa (2017). (f) Yu (2019). (g) Balasubramanian et al. (2020). (h) Jiang (2021). (i) This study. All points are color coded according to the predicted POC/SPM from our green band POC/SPM algorithm.

Figure 12. Comparison of Landsat-derived SPM and in situ measured SPM using the proposed SPM algorithm. The RMSE value was calculated using the original data, i.e., not in the log space.

Figure 13. Comparison of in situ-measured water turbidity and satellite-derived SPM in several selected sites. (a) East Coast, USA: Connecticut River. (b) Gulf of Mexico, USA: Atchafalaya. (c) West Coast, USA: San Francisco Bay. (d) Pacific Northwest, Canada: Taku River. (e) East Coast, USA: Back River. The left panel shows the time series of in situ turbidity measurement and satellite estimate of SPM, the right panel shows scatter plot of matchup data of in situ turbidity measurement and satellite estimate of SPM with data points color coded according to the satellite-derived POC/SPM using our green band POC/SPM algorithm. The LC09, LC08, and LE07 represent Landsat 9, 8 and 7, respectively.

Figure 14. Spatial pattern of Landsat 8-derived SPM. (a) Northeast US coast (March 21, 2021). (b) Mississippi River Delta (March 18, 2021). The insets on right hand side provide zoomed-in views of specific areas, illustrating finer details of the SPM pattern.

Figure 15. Seasonal variability of SPM over past 4 decades derived from Landsat 5, 7, 8, 9 over the period 1984-2024 for several coastal regions. The solid centerline refers to the median SPM. (a) San Francisco Bay. (b) North South River in northeastern US. (c) Atchafalaya Delta.

Figure 16. Sen's slope (g/m^3/year) of Landsat-derived SPM over the past four decades (1984 to 2023) (a) Atchafalaya River and Lake Pontchartrain. (c) Blackwater and Fishing Bay. Panels (b) and (d) display box plots of SPM at five-year intervals, illustrating temporal trends in SPM levels. The location of (b) and (d) are marked in the map (a).

Supplementary Figure S1. Comparison of satellite mission and sensor characteristics for the ocean color sensor (MODIS) on satellite Terra and Aqua missions and the land observation sensor on satellite Landsat missions. (a) Spectral coverage and resolution. (b) Operational period.

Supplementary Figure S2. Comparison of particle composition-specific algorithms for estimating SPM from remote-sensing reflectance R_{rs} for the organic-rich, mineral-rich, and extremely mineral-rich (E) particle composition classes. The left y-axis represents the reflectance at the red band used in the algorithm for the organic-rich class. The right y-axis represents reflectance at the NIR band used in the algorithms for the mineral-rich and extremely mineral-rich (E) classes.

Supplementary Figure S3. In situ measured R_{rs} vs. Landsat SR. (a) $R_{rs}(490)$ and SR Blue. (b) $R_{rs}(555)$ and SR Green. (c) $R_{rs}(670)$ and SR Red. (d) $R_{rs}(810)$ and SR NIR.

Supplementary Material

High Spatial-Resolution Satellite Mapping of Suspended Particulate Matter in Global Coastal Waters Using Particle Composition-Adaptive Algorithms

Wenxiu Teng [a*], Qian Yu [a], Dariusz Stramski [b], Rick A. Reynolds [b], Jonathan D. Woodruff [a], Brian Yellen [a]

[a] Department of Earth, Geographic, and Climate Sciences, University of Massachusetts Amherst, Amherst, MA, USA
[b] Marine Physical Laboratory, Scripps Institution of Oceanography, University of California San Diego, CA, USA

Corresponding author: Wenxiu Teng (wteng@umass.edu)

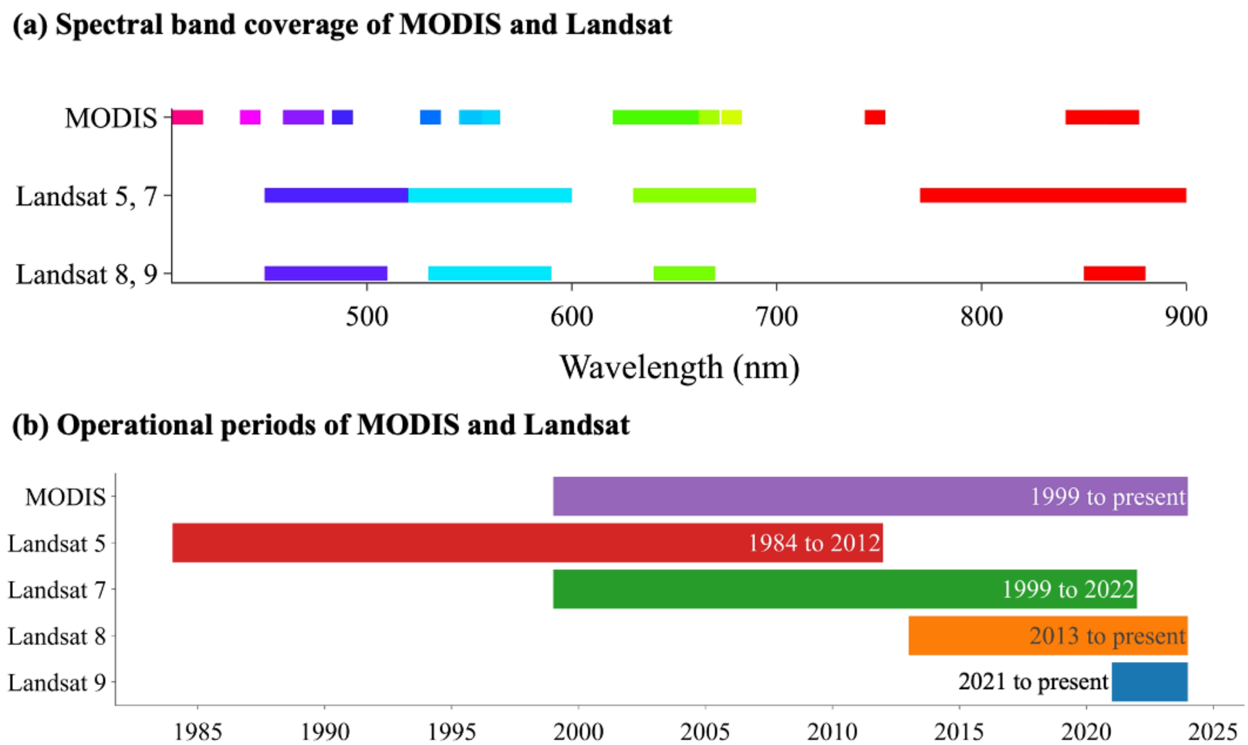

Supplementary Figure S1. Comparison of satellite mission and sensor characteristics for the ocean color sensor (MODIS) on satellite Terra and Aqua missions and the land observation sensor on satellite Landsat missions. (a) Spectral coverage and resolution. (b) Operational period.

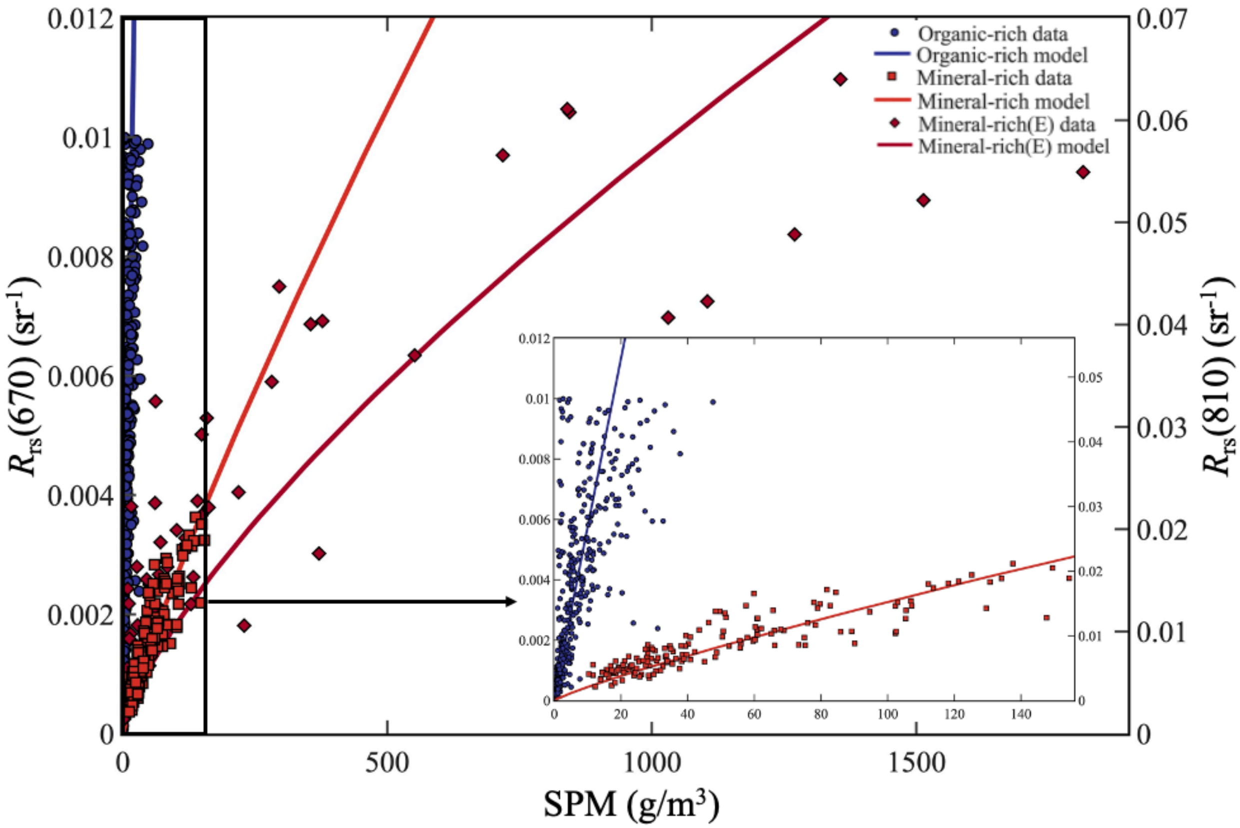

Supplementary Figure S2. Comparison of particle composition-specific algorithms for estimating SPM from remote-sensing reflectance R_{rs} for the organic-rich, mineral-rich, and extremely mineral-rich (E) particle composition classes. The left y-axis represents the reflectance at the red band used in the algorithm for the organic-rich class. The right y-axis represents reflectance at the NIR band used in the algorithms for the mineral-rich and extremely mineral-rich (E) classes.

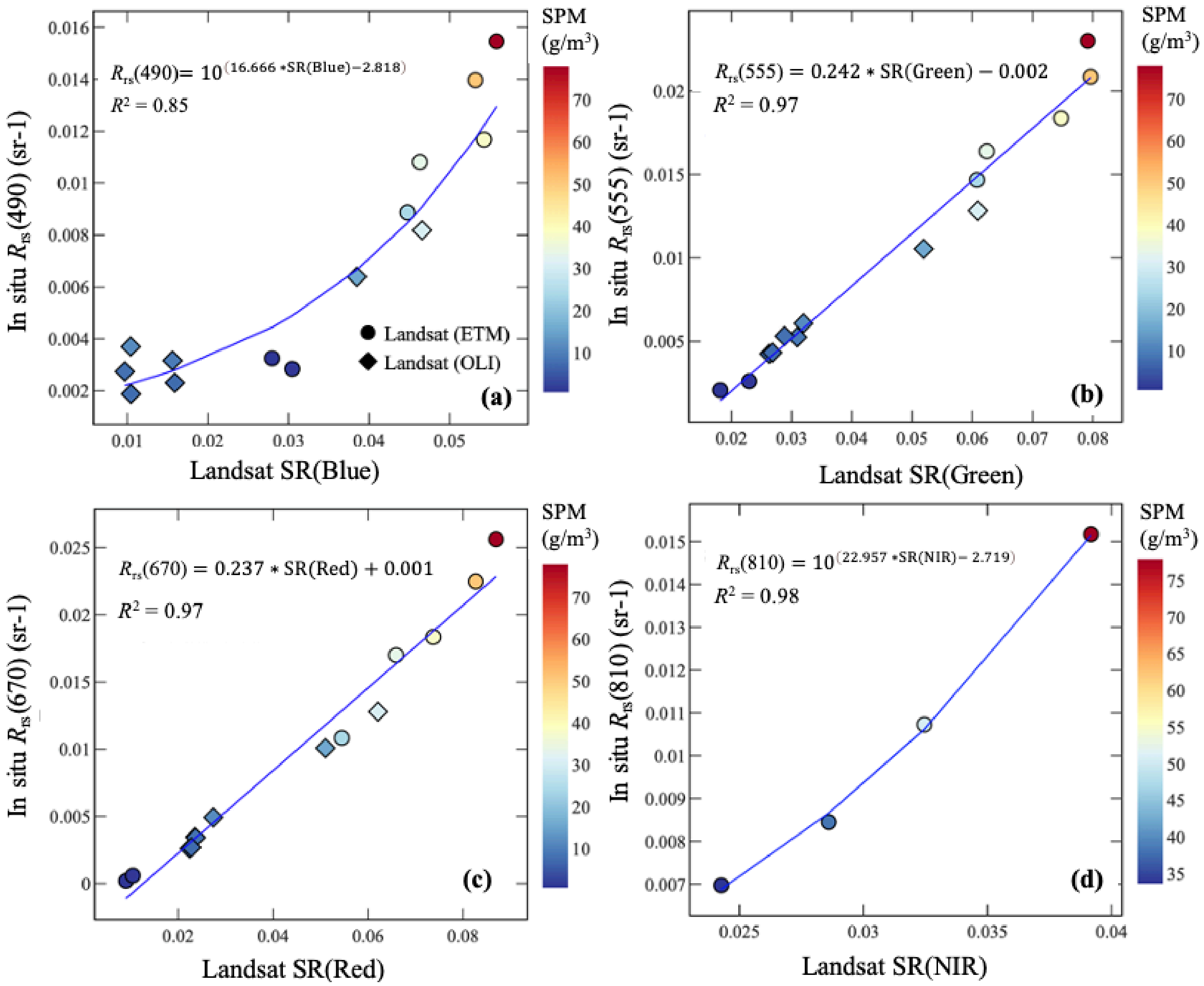

Supplementary Figure S3. In situ measured R_{rs} vs. Landsat SR. (a) $R_{rs}(490)$ and SR Blue. (b) $R_{rs}(555)$ and SR Green. (c) $R_{rs}(670)$ and SR Red. (d) $R_{rs}(810)$ and SR NIR.

Supplementary Table S1. Summary of optical wavelengths, water type classification criteria, algorithm type, and main equations for the algorithm proposed in this study and other previously published algorithms. Wavelengths marked with an asterisk (*) are not available on Landsat sensors.

Wavelengths	Water type classification criteria	Algorithm type	Main equations	Reference
551,862	-	Empirical	$\mathrm{TSM} = \exp\left(3.132 \cdot \frac{R_{\mathrm{rs}}(862)}{R_{\mathrm{rs}}(551)} + 3.01\right)$	Doxaran et al., 2002
668	-	Empirical	$\mathrm{TSM} = 1140.25 \cdot R_{\mathrm{rs}}(668) - 1.91$	Miller and McKee, 2004
665	-	Empirical	$\mathrm{TSM} = 1.74 + \frac{355.85 \cdot \pi \cdot R_{\mathrm{rs}}(665)}{1 - \frac{\pi \cdot R_{\mathrm{rs}}(665)}{1728}}$	Nechad et al., 2010
668	-	Empirical	$\mathrm{TSM} = 12450 \cdot R_{\mathrm{rs}}(668)^2 + 666.1 \cdot R_{\mathrm{rs}}(668) + 0.48$	Petus et al., 2010
561, 665 865	Green: $\rho_{\mathrm{w}}(665) < 0.007$ Green_Red: $0.007 \leq \rho_{\mathrm{w}}(665) \leq 0.016$ Red: $0.016 < \rho_{\mathrm{w}}(665) < 0.08$ Red_NIR: $0.08 \leq \rho_{\mathrm{w}}(665) \leq 0.12$ NIR: $\rho_{\mathrm{w}}(665) > 0.12$ $\rho_{\mathrm{w}}(\lambda)$ is water-leaving reflectance	Empirical	$C_{\mathrm{SPM\_Green}} = 96.6 \cdot \rho_w(561)$ $C_{\mathrm{SPM\_Green\text{-}Red}} = \alpha_1 \cdot C_{\mathrm{SPM\_Green}} + \beta_1 \cdot C_{\mathrm{SPM\_Red}}$ $C_{\mathrm{SPM\_Red}} = 575.8 \cdot \rho_w(665)$ $C_{\mathrm{SPM\_Red\text{-}NIR}} = \alpha_2 \cdot C_{\mathrm{SPM\_Red}} + \beta_2 \cdot C_{\mathrm{SPM\_NIR}}$ $C_{\mathrm{SPM\ NIR}} = 32110 \cdot \rho_w(865)^2 + 2204 \cdot \rho_w(865)$	Novoa et al., 2017
486, 551, 671, 745*, 862	-	Empirical	$GI_{SPM} = c_0 \cdot \frac{R_{\mathrm{rs}}(551)}{R_{\mathrm{rs}}(486)} + \sum_{i=1}^{3} c_i \cdot W_i \cdot \frac{R_{\mathrm{rs}}(\lambda_i)}{R_{\mathrm{rs}}(551)}$ $W_i = \frac{R_{\mathrm{rs}}(\lambda_i)}{R_{\mathrm{rs}}(\lambda_1) + R_{\mathrm{rs}}(\lambda_2) + R_{\mathrm{rs}}(\lambda_3)}, i = 1,2,3$ $C_{\mathrm{SPM}} = a_1 \cdot [GI_{\mathrm{SPM}}]^{a_2}$	Yu et al., 2019
443, 482, 561, 655, 865	Type II: $R_{\mathrm{rs}}(665) < R_{\mathrm{rs}}(560)$ & $R_{\mathrm{rs}}(665) > R_{\mathrm{rs}}(492)$ Type III: $R_{\mathrm{rs}}(665) > R_{\mathrm{rs}}(560)$ & $R_{\mathrm{rs}}(740) < 0.01\ \mathrm{sr}^{-1}$ Type I: $R_{\mathrm{rs}}(560) < R_{\mathrm{rs}}(492)$ Type II: $R_{\mathrm{rs}}(560) \geq R_{\mathrm{rs}}(492)$	semi-analytical, machine learning, and empirical models	$\mathrm{TSS}_{\mathrm{Type\ I}} = 53.736 \cdot b_{\mathrm{bp}}(665)^{0.8559}$ $\mathrm{TSS}_{\mathrm{Type\ II}} = 53.736 \cdot b_{\mathrm{bp}}(665)^{0.8559}$ $\mathrm{TSS}_{\mathrm{Type\ III}} = (207.57 \cdot b_{\mathrm{bp}}(740)) - 46.78$	Balasubramanian et al., 2020
443, 490, 560, 620*, 665, 754*, 865	Type I: $R_{\mathrm{rs}}(490) > R_{\mathrm{rs}}(560)$ Type II: $R_{\mathrm{rs}}(490) > R_{\mathrm{rs}}(620)$ Type IV: $R_{\mathrm{rs}}(754) > R_{\mathrm{rs}}(490)$ & $R_{\mathrm{rs}}(754) > 0.01\ \mathrm{sr}^{-1}$ Type III: Other	semi-analytical	$\mathrm{TSS}_{\mathrm{Type\ I}} = 94.607 \cdot b_{\mathrm{bp}}(560)$ $\mathrm{TSS}_{\mathrm{Type\ II}} = 114.012 \cdot b_{\mathrm{bp}}(665)$ $\mathrm{TSS}_{\mathrm{Type\ III}} = 137.665 \cdot b_{\mathrm{bp}}(754)$ $\mathrm{TSS}_{\mathrm{Type\ IV}} = 166.168 \cdot b_{\mathrm{bp}}(865)$	Jiang et al., 2021
555, 670, 810	Organic-rich: POC/SPM > 0.12 or $R_{\mathrm{rs}}(670) < 0.01\ \mathrm{sr}^{-1}$ Mineral-rich: 0.02 < POC/SPM < 0.12 Mineral-rich (E): POC/SPM < 0.02	Empirical	$\frac{\mathrm{POC}}{\mathrm{SPM}} = 10^{(-0.973 * G - 3.323)}$ $\mathrm{SPM}_{\mathrm{org}} = 1992.2 \cdot R_{\mathrm{rs}}(\lambda_{Red})^{1.027}$ $\mathrm{SPM}_{\mathrm{min}} = 12662.7 \cdot R_{\mathrm{rs}}(\lambda_{NIR})^{1.157}$ $\mathrm{SPM}_{\mathrm{min(E)}} = 50556.7 \cdot R_{\mathrm{rs}}(\lambda_{NIR})^{1.371}$	This study